HYDROLOGY OF SMALL RESERVOIRS IN SEMI-ARID NORTHERN GHANA

A Dissertation

Presented to the Faculty of the Graduate School

of Cornell University

in Partial Fulfillment of the Requirements for the Degree of

Doctor of Philosophy

by

Jens Reiner Liebe

January 2009

HYDROLOGY OF SMALL RESERVOIRS IN SEMI-ARID NORTHERN GHANA

Jens Reiner Liebe, Ph.D.

Cornell University 2009

This thesis analyzes the suitability of radar satellite images for monitoring small reservoir surfaces, the suitability of remotely sensed time series of their surface areas to calibrate hydrological models, and small reservoir evaporation losses.

Radar remote sensing of small reservoirs is suitable especially during the rainy season, but is affected by wind and lack of vegetation context during the dry season. Reservoirs could be extracted from the radar images most often with a quasi-manual classification approach, as stringent classification rules often failed under less than optimal conditions. Failure to extract reservoirs was due to the backscattered radar signal that occurred above wind speeds of 2.6 m s^{-1} (Bragg scattering). Due to lower wind speeds, the use of night time acquisitions was more effective than the use of daytime images. As optical systems perform well under low vegetation contrast, and independent of wind conditions, radar and optical systems can be used complimentary.

Time series of remotely sensed small reservoir surface areas, translated into storage volume changes, were successfully used to calibrate hydrological rainfall-runoff models. Eight small reservoirs in the Upper East Region of Ghana, and Togo, were monitored to calibrate modified Thornthwaite-Mather models, in which increasing precipitation leads to exponentially increasing contributing areas. The model results indicate that the overall impact of the reservoirs largely depends on the ratios of reservoir and watershed areas. For this

two year study, the reservoirs captured on the average 34% of quick flow, and 15% of overall watershed runoff.

Reservoir evaporation losses were measured directly with a floating evaporation pan (E_o) and were compared to evaporation rates determined from the reservoir's energy budget (E_B) and Penman's equation (E_t). The direct E_o measurements were generally lower than E_t and E_B. Compared to land based $E_{t\ Land}$, the reservoir evaporation E_t was not excessive. Regional wind patterns influence evaporation dynamics from the reservoir. Northeast winds with a high saturation deficit lead to significant evaporation losses, while the evaporation losses under moister, more prevalent southwest winds were moderate.

BIOGRAPHICAL SKETCH

Jens Reiner Liebe was born in Kirchheim unter Teck, Germany, in 1975. After he graduated from Schloßgymnasium Kirchheim in 1995, he enrolled at the University of Heidelberg to study Geography, Geology, and Political Science. Two years later, he transferred to the University of Bonn, where he received a M.Sc. in Geography (Diplom-Geograph), with minors in Geology and Soil Science in 2002. During his time at the University of Bonn, he worked and traveled in East, Southern, and West Africa, and became interested in the hydrology of semi-arid areas, and the capabilities of remote sensing in data scarce areas. In January 2004, Jens joined Cornell University to start his Ph.D. program at the Department of Biological and Environmental Engineering.

To my parents, Andrea and Reiner.

ACKNOWLEDGEMENTS

This work would not have been possible without the dedication and support of numerous people. First of all I would like to thank Tammo Steenhuis and my committee members M. Todd Walter and Lawrence Cathles for their support, the many hours of help and discussions, sound advice, and lots of good ideas. I would also like to thank my external committee members Marc Andreini, and Nick van de Giesen. I am especially grateful to Nick van de Giesen, who has been an inspiration for the last ten years.

This research was conducted within the Small Reservoirs Project, which is funded through the Challenge Program on Water and Food (CP46). Beyond my immediate work partners with whom I have enjoyed interactions, and learned from, are all the SRP team members, Marc Andreini, Nick van de Giesen, Winston Andah, Eileen Boelee, Hammou Lamrani, Philippe Cecchi, Annette Huber-Lee, Lineu Neiva Rodrigues, Aidan Senzanje, and Tonya Schütz.

I gratefully acknowledge the co-operation with the GLOWA-Volta Project, the Center for Development Research at the University of Bonn, Germany, and the International Water Management Institute (IWMI), Ghana, for supporting the field work. I am especially grateful to Dr. Boubacar Barry from the International Water Management Institute in Ghana, for his support with logistics, his expertise, and good humor.

The field work would not have been successful without the help of my assistant, Isaak Agbango, the former Assemblyman Honorable Sandow Uben Nkruma, and the many helpers. I owe special thanks to the multi-talented drivers I have worked with over the last few years: Eli Ellis Sokpoli, and David Kwesi Orchard, and Salisu Adam.

I am also grateful to Kees van Beek from the Technical University of Delft for developing the custom data logger and pump control used with the floating evaporation pan, and my friend Jan Friesen, also at TU Delft, for help and support with field work, advice for programming, and an innumerable amount of favors granted during the course of this research. Satellite data was obtained from the European Space Agency (ESA) as principal investigator 2315, and through ESA's Tiger Project 2871.

Finally, I want to thank my family and friends, and especially my partner Kimberly, for their support and encouragement over the years.

TABLE OF CONTENTS

Biographical Sketch . . . iii
Dedication . . . iv
Acknowledgements . . . v
Table of Contents . . . vii
List of Tables . . . ix
List of Figures . . . x

1 SUITABILITY AND LIMITATIONS OF ENVISAT ASAR FOR MONITORING SMALL RESERVOIRS IN A SEMIARID AREA 1
1.1 Introduction . . . 1
1.2 Radar remote-sensing of open water . . . 3
1.3 Study Region . . . 6
1.4 Data sets and methods . . . 8
1.4.1 Reservoir bathymetry and areas . . . 8
1.4.2 Wind speed and wind direction data . . . 9
1.4.3 ENVISAT Satellite Data . . . 9
1.4.4 Classification of small reservoir surface areas . . . 10
1.5 Results . . . 12
1.5.1 Reservoir classification . . . 12
1.5.2 Comparison of radar based and bathymetry based reservoir sizes . . . 18
1.5.3 Wind speeds and scene acquisition times . . . 22
1.6 Discussion . . . 23
1.7 Conclusion . . . 27

REFERENCES 30

2 DETERMINING WATERSHED RESPONSE IN DATA POOR ENVIRONMENTS WITH REMOTELY SENSED SMALL RESERVOIRS AS RUNOFF GAUGES 33
2.1 Introduction . . . 33
2.2 Study Area and Hydrology . . . 35
2.3 Materials and Methods . . . 36
2.4 Observed Runoff Calculations . . . 38
2.5 Runoff Model . . . 40
2.5.1 Calibration and Validation . . . 45
2.6 Results . . . 46
2.6.1 Reservoir and watershed sizes . . . 46
2.6.2 Rainfall Characteristics . . . 48
2.6.3 Rainfall-Runoff Relationships . . . 49
2.7 Discussion . . . 51
2.8 Conclusion . . . 54

REFERENCES **55**

3 Local and regional controls on evaporation from a small reservoir in Ghana **59**

3.1 Introduction 59
3.2 Site Monitoring 60
3.3 Evaporation Calculations 63
3.3.1 Pan evaporation 63
3.3.2 Reservoir Energy Balance 63
3.3.3 Penman evaporation from weather station data, and absolute humidity 65
3.3.4 Energy advection 66
3.4 Results 67
3.4.1 Floating pan evaporation, E_o 67
3.4.2 Reservoir Energy balance, E_B, and Penman E_t 68
3.5 Discussion 70
3.5.1 Comparison of E_o, E_B, and E_t 70
3.5.2 Comparison of reservoir surface water temperature, and pan water temperature 71
3.5.3 Upwind and downwind effects at weather stations 73
3.6 Conclusion 78

REFERENCES **80**

LIST OF TABLES

1.1 ENVISAT acquisition characteristics, average wind data, and bragg criteria 19

2.1 Penman reference evaporation rates from long term averages (1961-1990) for the Meteorological Station Navrongo (10°53'1" N, 1°5'4" W, 201.3 m asl) 38
2.2 Reservoir surface areas [ha] classified from ENVISAT ASAR images. 47
2.3 Measured watershed area and calibrated root zone storage, S_{max} and watershed contributing factor, '*a*'. 47

3.1 Components of the reservoir's energy budget, E_o, E_B, Penman E_t over water, and Penman $E_{t\ Land}$. 69

LIST OF FIGURES

1.1 Location of the three reservoirs, and weather stations within the Tanga watershed, in the Upper East Region of Ghana. Weather stations recording wind speed and direction are located on Reservoir 3. 7
1.2 Example of a training area (a), and resulting reservoir area after growing by 3.1 standard deviations (b) 11
1.3 ENVISAT ASAR bands and scatterplots for September 2, 2005 (a-d), and September 19, 2005 (e-h). 13
1.4 Classification results on Reservoir 3 14
1.5 ENVISAT ASAR bands and scatterplot from April 20, 2006 (a-d) 17
1.6 Histogram analysis 20
1.7 Comparison of reservoir sizes based on bathymetry and water level measurements to reservoir sizes determined with ENVISAT. 21
1.8 Measured wind speeds over the course of the year for morning (magenta, 10-day averages in red) and evening overpasses (dark blue, 10-day averages in light blue), and the wind speed Bragg criterion (orange). 23
1.9 Comparison of reservoir sizes from ENVISAT classification (markers) with reservoir sizes from bathymetrical models (lines) 26

2.1 Location of eight reservoirs (dots) and the associated watersheds (shaded) in the eastern part of the Upper East Region of Ghana, and Togo. 36
2.2 Evolution of the water volume in Reservoir 2 during the 2005 rainy season. 41
2.3 Quickflow, Q_f, as a function of the effective rainfall, P^*, for different watershed factors '*a*' (Equation 2.14) 44
2.4 Example of Reservoir 6, 2005, for the calculations to determine the maximum storage of the root zone, S_{max}, and the watershed parameter, '*a*', that determines the rate that the saturated areas are expanding. 45
2.5 Normalized precipitation patterns (black bars), scaled from 0 to 1 with respect to the maximum rainfall event observed within the two years (min 45 mm, max 66 mm, avg. 56.6 mm), and occurrence of *'wet days'* (gray) according to Equation 2.2 for the 8 reservoirs in 2005 and 2006. 48
2.6 Observed (triangles) and predicted (bold lines) cumulative quick flow (Equation 2.14), moisture deficit (gray line, defined as $E_{act} - E_{pot}$), effective rainfall (P^*), and precipitation (black bars) for reservoir 2. (a) Calibrated model in 2005 (S_{max} =42.5 mm; '*a*' = 0.025) and (b) Validated model in 2006. 50

2.7 Observed and predicted cumulative runoff in the calibration year 2005 (left, r^2=0.83) and the validation year 2006 (right, r^2=0.92). 51
2.8 Impact of reservoirs on water resources (quickflow, Q_f, and ground water, *GW*). 53

3.1 Study site and experimental setup. 60
3.2 Automated floating evaporation pan. 61
3.3 Daily floating pan evaporation (heavy black lines), and average daily precipitation (grey vertical lines) during the study period. . 67
3.4 Comparison of daily E_o with E_B (x's), and E_t (dots) 70
3.5 Comparison of daily E_B and E_t for the reservoir at WS_{FP} 71
3.6 Comparison of daily E_t over water (at WS_{FP}) with E_t over land (at WS_{SE2}) 72
3.7 Pan water (hourly in dark red, 24h moving average in red) and reservoir surface water (hourly in light blue, 24h moving average in dark blue) temperatures. 73
3.8 The effect of surface water and pan water temperature on E_B. . . 74
3.9 Local wind direction and speed prevalence patterns. The length of wind rose wedges correspond to the prevalence of wind from that direction. The colored subsections indicate wind speed frequencies. 75
3.10 *aH* scatterplot (a) and saturation deficit (b) when WS_{NW} is in upwind position of WS_{FP} (cirlce in (b)). 76
3.11 *aH* scatterplot (a) and saturation deficit (b) when WS_{SW} is in downwind position of WS_{FP} (cirlce in (b)). 77
3.12 *aH* scatterplot (a) and saturation deficit (b) when WS_{SW} is in upwind position of WS_{FP} (cirlce in (b)). 78

CHAPTER 1

SUITABILITY AND LIMITATIONS OF ENVISAT ASAR FOR MONITORING SMALL RESERVOIRS IN A SEMIARID AREA

1.1 Introduction

In many semi-arid regions of the developing world, access to reliable water sources is the single most important factor for the agricultural economy. Thousands of small reservoirs dot the landscape, providing large volume water supply at the village level, improving food security, and stimulating economic development, especially in rural areas.

Small reservoirs have been largely neglected in hydrological and water resources research because of the combination of several key characteristics: small size, existence in large numbers, and widespread distribution. These characteristics constitute their main advantages for the scattered rural population but make their monitoring difficult. Adequate ground-based data on small reservoir storage volumes are commonly not available and conducting ground based surveys and measurements are prohibitively expensive and time consuming on a regional scale. To overcome the lack of baseline data, Liebe et al. (2005) classified the extent of small reservoir surface areas from Landsat ETM imagery, and determined regional small reservoir storage volumes with a regional area-volume equation. Recently, further studies on regional area-volume relations of small reservoirs have been published, i.e. (Cecchi, 2007; Sawunyama et al., 2006), indicating an interest in information on small reservoir storage volumes. Such regional storage volume estimates, however, depend on the ability to extract reservoir surface areas from satellite images. Optical satellite data yield

good results in delineating small reservoir surface areas under cloud-free conditions, but the often-cloudy conditions inhibit their use in an operational setting.

Although radar images, especially in C-band such as ENVISAT's Advanced Synthetic Aperture Radar (ASAR), have become routinely available, the classification of distributed inland water bodies has hardly been studied. Radar remote sensing is capable of penetrating clouds, and is seen as a promising alternative to optical sensors. Successful application of radar in determining small reservoir extents would not only facilitate transferring this methodology to other areas for regional assessment of small reservoir storage, but also allow regional monitoring of storage volumes.

This paper analyzes the suitability and limitations of radar remote sensing to determine small reservoir surface areas from a sequence of 22 ENVISAT ASAR images acquired bi-monthly from June 2005 until August 2006. In contrast to the common analysis of single images, or image pairs, this larger image sequence ensures taking into account the seasonal variations, i.e. the changing vegetation context, and the large variability of backscatter from water surfaces, i.e. through wind induced roughness. The surface areas are extracted from the image sequence for three reservoirs in the Upper East Region of Ghana, and compared to in-situ measurements based on bathymetric reservoir models and water level measurements.

Although radar images, especially in C-band such as ENVISAT's Advanced Synthetic Aperture Radar (ASAR), have become routinely available, the classification of distributed inland water bodies has hardly been studied. Radar remote sensing is capable of penetrating clouds, and is seen as a promising alternative to optical sensors. Successful application of radar in determining small reser-

voir extents would not only facilitate transferring this methodology to other areas for regional assessment of small reservoir storage, but also allow regional monitoring of storage volumes.

This paper analyzes the suitability and limitations of radar remote sensing to determine small reservoir surface areas from a sequence of 22 ENVISAT ASAR images acquired bi-monthly from June 2005 until August 2006. In contrast to the common analysis of single images, or image pairs, this larger image sequence ensures taking into account the seasonal variations, i.e. the changing vegetation context, and the large variability of backscatter from water surfaces, i.e. through wind induced roughness. The surface areas are extracted from the image sequence for three reservoirs in the Upper East Region of Ghana, and compared to in-situ measurements based on bathymetric reservoir models and water level measurements.

1.2 Radar remote-sensing of open water

The detection of surface water on radar images is usually described as a simple task (Henderson and Lewis, 1998). Smooth water surfaces act as specular reflectors and reflect most of the incoming radar signal away from the sensor. This is equivalent to very low radar backscatter signal returning to the sensor, which makes surface water bodies usually appear dark on radar images. This, however, is an oversimplification (Henderson, 1995), as the surface roughness of water bodies is very variable, both spatially, within a water body, and temporally, leading to a wide range of backscatter. As will be shown here, this variability in backscatter can greatly affect the operational value of radar images

for monitoring of small reservoirs. It is necessary to understand in some detail how contrast in backscatter between open water and surrounding land surface changes as a function of wind speed and direction, and vegetation density.

Wind induced, regularly spaced waves and ripples can lead to Bragg scattering (Valenzuela, 1978) which results in elevated backscatter signals from the water surface. While wave crests oriented orthogonally to the look direction can produce Bragg scattering, wave crests oriented in line with the look direction may have no significant effect on the radar backscatter. The threshold wind speed value causing Bragg scattering in C-band is estimated to be at ≈ 3.3 m s^{-1} at 10 m above the surface (ESA, 2005). This corresponds to a wind speed of 2.6 m s^{-1} at 2 m, using Sutton's (Sutton, 1934) equation for wind speed profiles.

Literature on open water delineation focuses on flood detection and presents various methods. Henderson (1995) presented a study on the extraction of lakes from X-Band radar in different environments, using manual interpretation to allow the inclusion of context and other interpretation clues in the analysis. Barber et al. (1996), and Brakenridge et al. (1994), visually interpret flood extents for the 1993 Assiniboine River flood in Manitoba, Canada, and the 1993 Mississippi River flood, respectively. Henry et al. (2006) use band thresholds to classify inundated areas of the 2002 Elbe river flood. Likewise, Brivio et al. (2002) map the extent of the flooded areas of the 1994 flood in the Regione Piemonte, Italy, based on visual interpretation and band thresholds. van de Giesen (2001) mapped flooding in a West African floodplain during the dry and wet seasons with L- and C-band SIR images, distinguishing between open water and water with reeds. Nico et al. (2000) compare flood detection from amplitude change detection to coherence methods from multi-pass Synthetic

Aperture Radar (SAR) data. Horritt et al. (2001) use a statistical active contour model to delineate flood boundaries, and Heremans et al. (2003) compare flood delineation results from and active contour model to that of an object oriented classification technique. Context is an important factor for the delineation of water bodies. The degree of accuracy that small water bodies can be extracted from the radar images largely depends on the land-water contrast. For a distinct land-water contrast, a low and coherent backscatter from the water body is desirable that stands in distinct contrast to its surroundings, ideally producing higher signal returns.

Due to the high dielectric constant of water, the penetration depth of the radar signal into the water, and hence volume scattering and depolarization is low (Henderson and Lewis, 1998). Reflections off of the water surface are thus predominantly like-polarized. The return from the water bodies in the HV band is therefore expected to be low. Tall reeds growing on the sides of the reservoirs during the rainy season can act as corner reflectors, which lead to high backscatter signals in radar images due to double bounces which also can partially depolarize the radar signal (Henderson and Lewis, 1998). In the radar image this accentuates the land-water boundary and facilitates its detection (Henderson, 1995). In the HH band, water bodies can also be classified well when the water surface acts as a specular reflector, i.e. ideally under calm conditions. The vast portion of the radar burst is then scattered away from the sensor, leaving the water body to appear dark in the image. Under windy conditions, however, a rough water surface reflects more of the incoming radar signal back to the sensor. These elevated returns under windy conditions, especially in the like-polarized bands, are again due to the high dielectric constant of water.

As wind speeds are not always uniform over the entire water body, elevated backscatter can occur in patches or affect larger parts of the reservoir. Although elevated backscatter from the water surface is detrimental to its classification in most cases, it can also be seen as a signal typical for water bodies, which can be helpful in classifying reservoirs. Images acquired in dual polarization mode can therefore provide further clues for the land-water separation. In general, like polarized images have a better overall image contrast (Henderson and Lewis, 1998), but VV is affected much more by Bragg scattering relative to the HH and HV response (Van der Sanden and Thomas, 2004).

In this paper, the different subtleties of open water delineation with ENVISAT ASAR will be explored, leading to a comprehensive overview of the strengths and drawbacks.

1.3 Study Region

The study is conducted in a 23 km^2 watershed surrounding the village of Tanga-Natinga in the Upper East Region of Ghana, West Africa (Figure 1.1). Three small reservoirs, referred to as Reservoirs 1, 2, and 3, supply the population of the villages of Tanga, Weega, and Toende with water for irrigation and gardening, livestock watering, household use, building, and fishing (Faulkner et al., 2008; Liebe et al., 2007). Maximum depths are 5.2 m for Reservoir 1, 4.7 m for Reservoir 2, and 4.3 m for Reservoir 3. Climatically, the research area is located in the semi-arid tropics, and is characterized by a mono-modal rainy season from July to September, with 986 mm of average annual rainfall, and 2,050 mm of average annual potential evaporation (Kranjac-Berisajevic et al., 1998). The

area lies in the northern Guinea savanna zone, and the vegetation is characterized by open woodland, interspersed with annual grasses (Windmeijer and Andriesse, 1993). Due to high population pressure, large areas are under agricultural use. Between reservoirs and agricultural land, there is usually a grass buffer of 10-30 m.

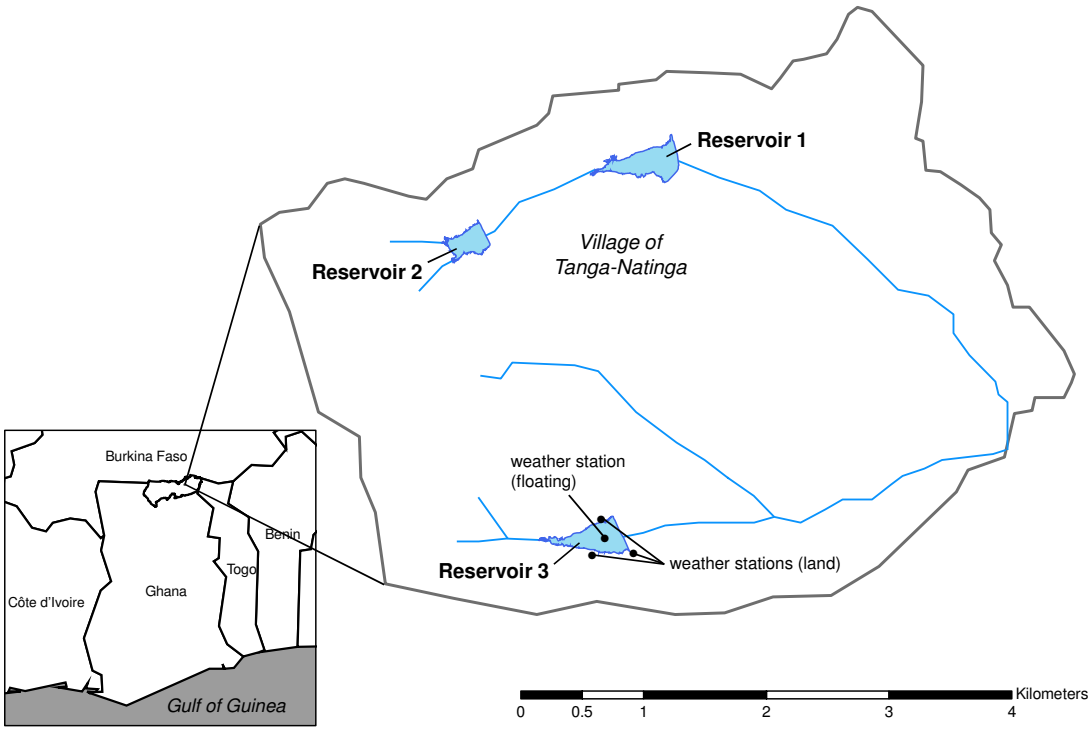

Figure 1.1: Location of the three reservoirs, and weather stations within the Tanga watershed, in the Upper East Region of Ghana. Weather stations recording wind speed and direction are located on Reservoir 3.

The vegetation dynamics in the vicinity of the reservoirs are largely driven by the rainfall patterns. After the first rains, grasses grow around the reservoirs. During the rainy season, the grasses can grow up to 2 m tall, and extensive reeds are found in the tail parts of the reservoirs. In the dry season, the grasses

are often harvested for roofing material etc., burned, or they deteriorate, leaving behind bare, dry, soil with sparse knee-high grass tussocks as vegetation. The direct vicinity of the reservoirs is then free of vegetation, exposing the bare banks of the reservoirs.

1.4 Data sets and methods

1.4.1 Reservoir bathymetry and areas

Bathymetric reservoir models and water level measurements serve as ground reference data for comparison with reservoir surface areas determined with ENVISAT images. The bathymetric models were generated from GPS tagged water depth measurements and reservoir outlines as described in Liebe et al. (2005). Water level measurements are used together with the bathymetric models to determine the surface area and storage volumes of the reservoirs.

Water levels were measured with pressure transducers at 15 minute intervals. These were used to determine ground reference data of reservoir surface areas at the time of image acquisition, which are compared to the radar based results. For Reservoirs 1 and 2, water level data are available from 6 June 2005 until 21 February 2006, and for Reservoir 3 from 6 June 2005 until 3 August 2006.

1.4.2 Wind speed and wind direction data

Wind induced waves and ripples may influence the radar signal return from water surfaces. Besides wind speed, the wind direction is of importance, as it determines the crest orientation of the wind induced waves. Assuming that wind produces waves with crests orthogonal to the wind direction, high wind speeds with wind directions orthogonally to the look direction may affect the backscatter from the water bodies less than wind directions in line with the look direction. Wind speed was measured on the center of Reservoir 3 and is available from October 2005 onward. In addition, wind speed and wind direction were measured at three locations on the shore of Reservoir 3 (Figure 1.1) at two minute intervals, starting in August 2005.

1.4.3 ENVISAT Satellite Data

In this study, 22 ENVISAT ASAR acquisitions are used with a roughly bi-monthly coverage from June 2005 until August 2006. ENVISAT ASAR is a C-band radar. We used APG images, with a nominal spatial resolution of 30 m, and a pixel spacing of 12.5 m. ENVISAT's ASAR instrument can acquire images in dual polarization mode, and produce HH and VV, HH and HV, or VV and VH polarized image pairs (Gardini et al., 1995). In this study, we have chosen dual polarized acquisitions with the band combinations HH and HV. This combination has also been found useful in flood delineation by Henry et al. (2006). The scenes were acquired from different swaths (IS1 to IS6) with incidence angles ranging from an overall minimum of 12.57° to a maximum of 43.77° throughout the scenes. The look direction is 81.45° on ascending, and 261.45° on descending

images. Images were acquired in both ascending (night time acquisition) and descending (morning acquisition) nodes to take into account the diurnal wind patterns, which determine the occurrence of Bragg scattering.

1.4.4 Classification of small reservoir surface areas

Several approaches were tested to determine the surface areas of the reservoirs, such as the active contour method or snake algorithm (Xu and Prince, 1998), band thresholds, and classification on HV-HH scatterplots. None perform well on images with less than optimal land-water contrast, and/or water surfaces with patches of different backscatter intensities. Therefore we used a quasi-manual method to determine reservoir sizes.

In this quasi-manual method, a reservoir's radar signal is classified by digitizing a training area within the reservoir and growing the region to neighboring pixels using a threshold specified by increments of standard deviations from the mean value of the radar signal within these digitized training areas. The training areas were defined by digitizing a polygon on the water surface not affected by wind induced roughness (e.g., Figure 1.2 a). The standard deviations chosen for growing the regions from the digitized area vary for each reservoir and acquisition, and were chosen to grow the region to the shoreline. Generally, the number of standard deviations for growing the training areas are the higher, the better the contrast between land and water of the used band. The size of the training area can also have an influence on the standard deviations chosen for growing, depending on the variability of the backscatter values covered in the training area. Although there is no common rule, it may be noted that the

standard deviations used for growing the reservoir areas ranged from 1.0 to 7.8. The resulting reservoir areas often contain holes, but only areas defined by the boundaries of the reservoirs were considered. Figure 1.2 b shows the result for growing the above defined training area by 3.1 standard deviations on the HV band acquired on 2 September 2005.

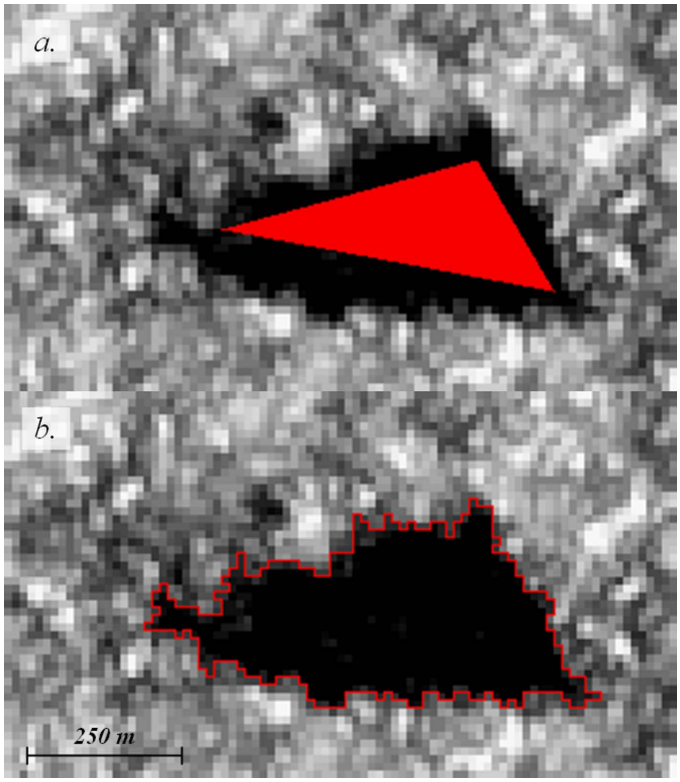

Figure 1.2: Example of a training area (a), and resulting reservoir area after growing by 3.1 standard deviations (b)

Due to the variability of the backscatter from the water bodies, and the variable land-water contrast, the band or band combinations with the best visual land-water contrast were chosen for the classification. The reservoirs were classified on either the HV or HH band alone, or an image generated by multiplying the bands $-1\times(HV\times HH)$, prior to classification.

1.5 Results

1.5.1 Reservoir classification

While some of the images clearly showed the reservoirs on both the HV and HH bands (e.g., Figure 1.3 a-b), often their visibility was drastically better in one of the bands (e.g., Figure 1.3 e-f). Given the large variability in radar backscatters from water surfaces, obtaining classification results from a large number of image acquisitions requires a relaxed classification scheme like the quasi-manual approach used here. The three following cases outline the importance of land-water-contrast, its variations, and the effect of incoherent backscatter from a water body.

An example of excellent contrast between land and water for both bands is the scene acquired on 2 September 2005. The water bodies appear dark in the images, have sharp borders, and can be classified from the low radar backscatter range of the HV and HH bands (Figure 1.3 a-b). At the time of image acquisition, weather station 1 recorded no wind, while the stations 2 and 3 recorded wind speeds of 1.3 m s^{-1}, and 3.0 m s^{-1}, respectively. The wind direction produced wave crests expected to be in line with the look direction (Figure 1.3 a, c), which is adverse to Bragg scattering, and therefore the water surface does not produce elevated backscatter. In Figure 1.3 d, ”water pixels” aggregate in a cluster with low HV and HH backscatter. Part of the reason the reservoirs in this image are so obvious is that during this part of the year the reservoirs are filled to their full extent and are flanked by tall vegetation. To delineate the water bodies, the active contour method (Figure 1.4 a), classification on the HH-HV scatterplot (Figure 1.4 b), and growing of a training area (Figure 1.4 c)

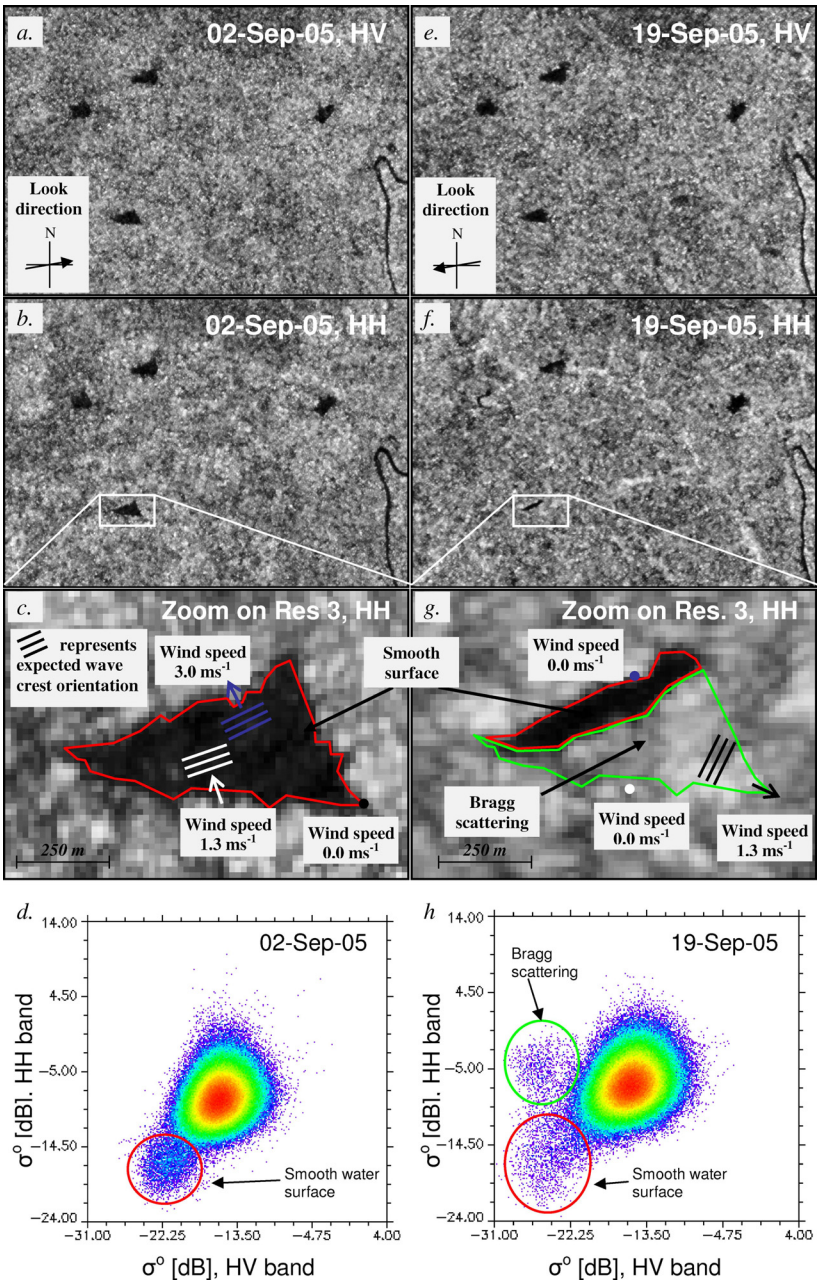

Figure 1.3: ENVISAT ASAR bands and scatterplots for September 2, 2005 (a-d), and September 19, 2005 (e-h).

HV band (a, e), HH band (b, f), and zoom on reservoir 3 in band HH (c, g), with wind speeds and directions (arrows), and expected crest orientation favorable for Bragg scattering. On September 2, the HV-HH scatterplot (d) shows a water cluster in the lower backscatter ranges. On September 19, a second cluster forms with low backscatter in HV (e) and elevated backscatter in HH (f) due to Bragg scattering in addition to the water cluster in the lower backscatter ranges.

all worked similarly well. Comparably excellent land-water contrast was only found in the image acquired on 7 October 2005, and less distinct, but still well on 11 July 2005, 29 July 2005, 28 November 2005, 11 July 2006, 3 August 2006, and 15 August 2006.

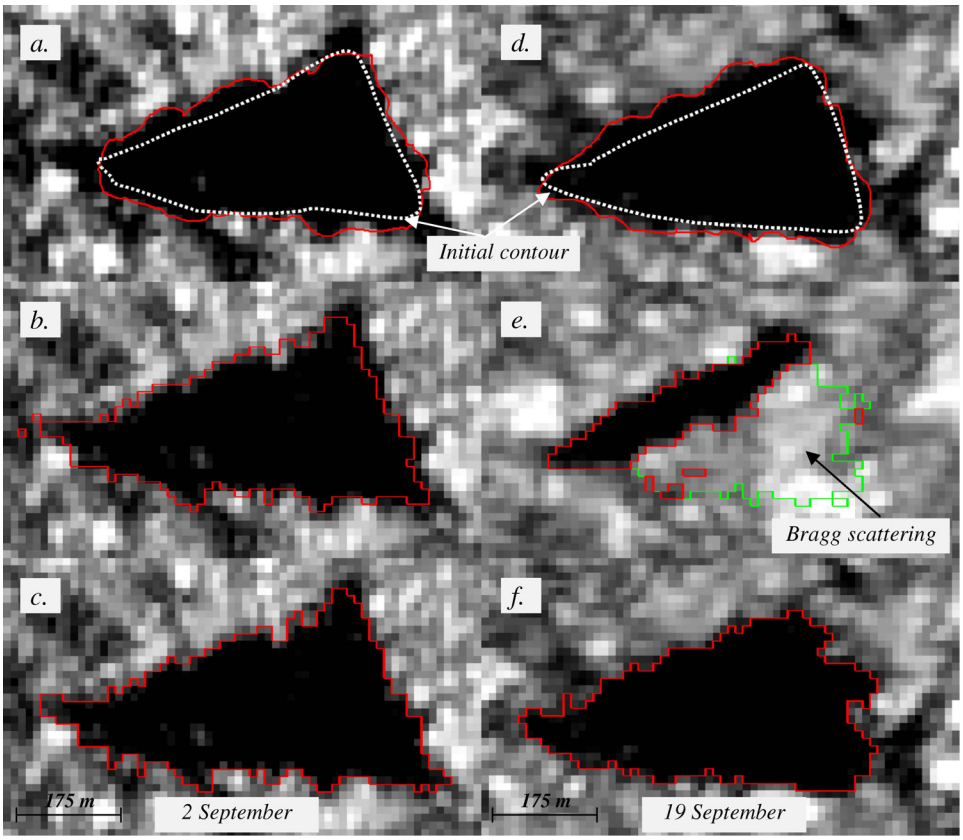

Figure 1.4: Classification results on Reservoir 3

left: 02 September 2005, (a) from active contour algorithm [Active contour parameters (Xu and Prince, 1998): Elasticity (alpha) = 0.1, Rigidity (beta) = 0.25, Viscosity (gamma) = 1.0, External Force (kappa) = 1.25, Gradient Scale Factor = 1.75, Delta Min (dmin) = 0.25, Delta Max (dmax) = 5.5, Noise Parameter (mu) = 0.1, GVF Iterations = 30, Contour Iterations = 120, Gaussian Sigma (sigma) = 1] on HH (11.3 ha), (b) from classification on the HH-HV scatterplot as outlined in Figure 1.4 a (11.3 ha), (c) from quasi-manual approach on HH (11.9 ha).
right: 19 September 2005, (d) from active contour algorithm on HV (11.4 ha), (e) from classification on the HH-HV scatterplot as outlined in Figure 1.4 (right) (3.7 (red) + 5.1 (green) = 8.8 ha, displayed on HH band), (f) from quasi-manual approach on HV (11.0 ha).

An example of an image that only shows the reservoirs well in one band was acquired on 19 September 2005. The land-water contrast is distinct in the HV band (Figure 1.3 e) but in the HH band (Figure 1.3 f) the major portions of the water surface of the Reservoirs 2 and 3, show elevated backscatter. While the vegetation surrounding the reservoirs is still as tall as on 2 September 2005, the reservoir outlines cannot be readily determined from the HH band (Figure 1.3 f-g). The elevated backscatter is likely to be caused by wind induced ripples. At the time the image was acquired, wind speeds of 1.3 m s^{-1} and gusts up to 1.86 m s^{-1} were measured at weather station 1. The wind direction recorded at weather station 1 produces wave crests expected to be roughly orthogonal to the look direction (Figure 1.3 e, g), a favorable constellation for Bragg scattering. While the water surface in the HV band does not seem to be affected, the surfaces of Reservoirs 2 and 3 (zoomed reservoir in Figure 1.3 g) are made up of two distinct patches; a dark strip on the windward side, where the wind may not have formed ripples yet, and elevated backscatter from the major part of the surface area towards the leeward side. In Figure 1.3 h., there are two distinctive clusters corresponding to open water. One cluster with low backscatter in both bands (red outlines), similar to Figure 1.3 d, and a cluster with low backscatter in the HV band, but elevated backscatter in band HH (green outlines in Figure 1.3 g; scatterplot in Figure 1.3 h) due to Bragg scattering. The active contour method (Figure 1.4 d) and growing of a training area method (Figure 1.4 f) still work well on the HV band, while the reservoir area obtained through combining the two clusters delineate in the HV-HH scatterplot (Figure 1.3 h) is too small (Figure 1.4 e). Good land-water contrast in the HV band and patches of both low backscatter and elevated Bragg scattering in the HH band are present in the acquisitions from 15 August 2005, 19 September 2005, and 24 October

2005. On the images acquired on 27 January 2006, 21 February 2006, 3 March 2006, and 13 June 2006 the land-water contrast was good in the HH band, and poorer in the HV band. This emphasizes the need for a flexible methodology for categorizing the parts of the radar images that correspond to reservoirs, i.e. one rigid method will incorrectly categorize the reservoir pixels on many of the images.

Figure 1.5 shows the same area on 20 April 2006 in which both bands fail to distinctly distinguish the water bodies from their surroundings. This image acquisition falls into the dry season when the reservoir levels and surface areas have decreased significantly and the water bodies are surrounded by previously water-covered, smooth, banks, which have a surface roughness similar to the water surface. The tall vegetation, which surrounded the reservoirs in the rainy season, is now essentially absent. Additionally, high wind speeds and wind directions favorable for generating wave crests orthogonally the look direction (Figure 1.5), and thus Bragg scattering, are recorded. The loss of land-water contrast in the dryer and less vegetated environment is reflected in the HV-HH scatterplot with the signal from water bodies scattered throughout (Figure 1.5).

Although we were unable to delineate the reservoirs in the images from 20 April 2006, we were able to do so for all the other acquisition days, even several images with similar contrast issues, e.g., images from 6 June 2005, 24 June 2005, 11 November 2005, 16 December 2005, 9 May 2006, and 29 June 2006.

In analogy to van de Giesen's 2001 flood plain analysis, image histogram characteristics were used for a qualitative image rating (Table 1.1). The band histograms were calculated for the zoom window on reservoir 3, for the extent as displayed in i.e. Figure 1.3 c. In cases of prononced land-water contrast in

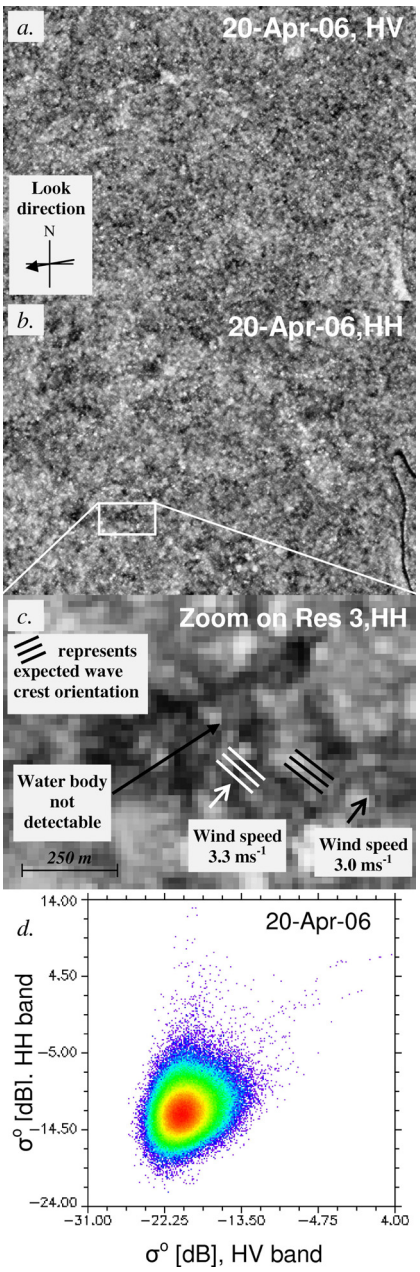

Figure 1.5: ENVISAT ASAR bands and scatterplot from April 20, 2006 (a-d)

HV band (a), HH band (b), and zoom on reservoir 3 in band HH (c), with wind speeds and directions (arrows; no record for weather station 2), and expected crest orientation of wind induced waves are favorable for Bragg scattering. The HV-HH scatterplot (d) shows no distinct water cluster that is different from the backscatter from the land.

a band, the histogram shows a double peak (Figure 1.6 a), where the peak in the lower backscatter range is due to the water body, and the peak at higher backscatter range is due to the vegetation. In bands with low or no land-water contrast the histogram produces only a single peak (Figure 1.6 b), where the water pixels and land pixels produced backscatter at similar intensities. Acquisitions with double peaks in both bands (i.e. Figure 1.6 b) were rated as "excellent" (*x*), while those acquisitions with a double peak in one band, and a single peak in the other band were rated as "good" (*g*). Acquisitions with single peaks in both bands histograms (i.e. Figure 1.6 b) were rated as "poor" (*p*) for land-water-separation.

The quasi-manual classification method has been arrived at through trial and error. The tested snake algorithm and band threshold approach gave very poor results on images with less than excellent land-water contrast, often not providing any sensible delineation. For this reason, no quantitative comparison of the different methods is provided.

1.5.2 Comparison of radar based and bathymetry based reservoir sizes

Reservoir surface areas could be extracted from 21 of the 22 ENVISAT scenes used in this study. These are compared to surface areas determined from the reservoirs' bathymetrical models, and water levels at the time of image acquisition. The overall performance of the reservoir size extraction compared well to bathymetry based reservoir sizes (r^2 = 0.92, Figure 1.7). The classification performance, however, varied for the individual reservoirs. The reservoir area

Table 1.1: ENVISAT acquisition characteristics, average wind data, and bragg criteria

Date	ENVISAT				Average Weather Station Data			
	Acquisition time	Look direction (°)	Histogram Peaks HV	Histogram Peaks HH	Land−water contrast*	Wind (ms^{-1})	Wind direction (°)	Wave crest orient.** (°)
06/06/2005	22:02	81.45	single	single	*p*	-	-	-
24/06/2005	9:56	261.45	single	single	*p*	-	-	-
11/07/2005	22:02	81.45	double	double	*x*	-	-	-
29/07/2005	9:56	261.45	double	double	*x*	-	-	-
15/08/2005	22:02	81.45	double	single	*g*	1.9	234.5	144.5
02/09/2005	9:56	261.45	double	double	*x*	1.4	158.0	68.0
19/09/2005	22:02	81.45	double	single	*g*	0.4	296.2	206.2
07/10/2005	9:56	261.45	double	double	*x*	0.6	195.1	105.1
24/10/2005	22:02	81.45	double	single	*g*	0.2	248.5	158.5
11/11/2005	9:56	261.45	single	single	*p*	4.6	79.1	169.1
28/11/2005	22:02	81.45	double	double	*x*	1.3	7.0	97.0
16/12/2005	9:56	261.45	single	single	*p*	3.6	15.7	105.7
27/01/2006	22:16	81.45	single	double	*g*	1.4	128.5	38.5
21/02/2006	9:51	261.45	single	double	*g*	3.1	31.4	121.4
03/03/2006	22:16	81.45	single	double	*g*	0.7	350.1	260.1
20/04/2006	22:08	81.45	single	single	n	3.2	219.7	129.7
09/05/2006	22:10	81.45	single	single	*p*	3.2	214.8	124.8
13/06/2006	22:10	81.45	single	double	*g*	1.6	270.3	180.3
29/06/2006	22:08	81.45	single	single	*p*	3.7	194.5	104.5
11/07/2006	9:51	261.45	double	double	*x*	3.9	227.5	137.5
03/08/2006	22:08	81.45	double	double	*x*	1.5	73.7	163.7
15/08/2006	9:51	261.45	double	double	*x*	1.6	219.0	129.0

* Land-water contrast rating based on categories described in 5.3. *x* = excellent, *g* = good, *p* = poor, *n* = none.
** assumed orthogonal to wind direction

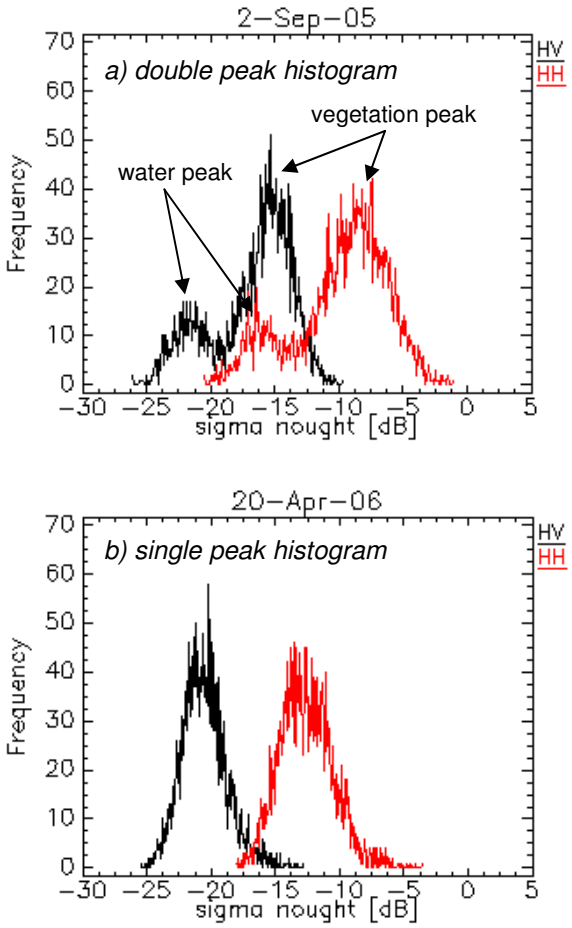

Figure 1.6: Histogram analysis

Figure 1.6 (a) Double peak histogram indicating excellent land-water contrast. Images with distinct land-water contrast show a double peak in the image histogram, here in both the HV and HH band. The extent of the analyzed window is shown in Figure 1.3 c

Figure 1.6 (b) Single peak histogram indicating poor land-water contrast. Images with poor or no land-water contrast only show a single peak in the image histogram, here in both the HV and HH band. The extent of the analyzed window is shown in Figure 1.5 c

classification of Reservoir 1 (r^2 = 0.83) is mainly affected by the extensive reeds found in the tail part of the reservoir. These are not identified as part of the water body, whereas they are included in the bathymetric model, causing a discrepancy. Reservoir 2 was the most difficult to classify. Its southern shore is composed of a very smooth, bare sandy loam, which diminishes the land-water contrast. Nevertheless, the highest coefficient of correlation was achieved for Reservoir 2 (r^2 = 0.95). Reservoir 3 was often affected by wind, which leads to patches of elevated backscatter. At greater fill levels, with surface areas over 10 ha, the discrepancies become larger (see also Figure 1.9).

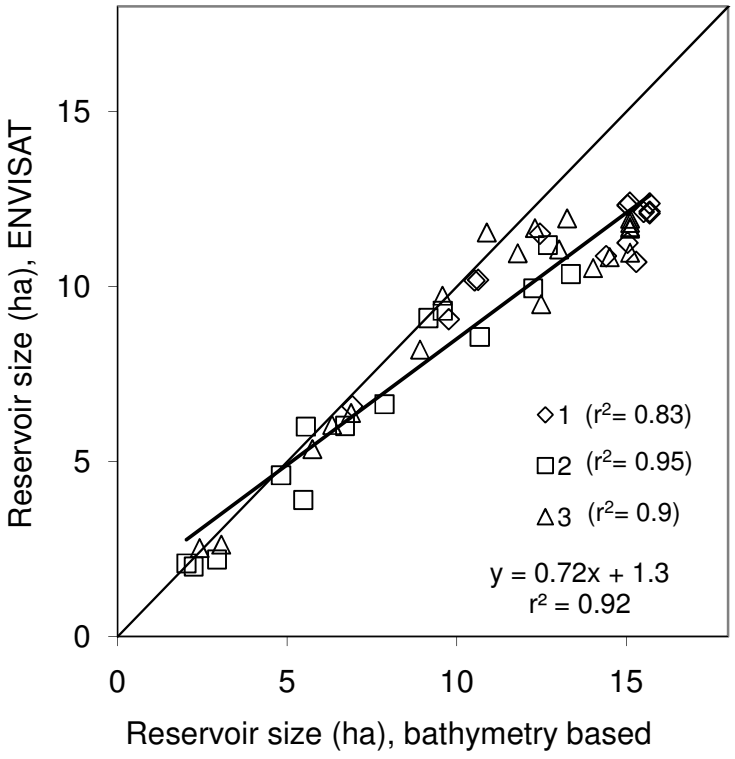

Figure 1.7: Comparison of reservoir sizes based on bathymetry and water level measurements to reservoir sizes determined with ENVISAT.

1.5.3 Wind speeds and scene acquisition times

The influence of wind speed at the time of image acquisition on the land-water contrast is apparent from the average wind speeds. Table 1 presents ENVISAT acquisition characteristics, and averaged wind speed and direction records. The acquisitions grouped in the above example of acquisitions with excellent land-water contrast (*'x'*, Table 1) are associated with wind speeds of 0.6, 1.3, 1.4, 1.5, 1.6, and 3.9 m s^{-1}, while images with good contrast but with some Bragg scattering effects (*'g'*, Table 1) show wind speeds of 0.2, 0.4, 0.7, 1.4, 1.6, 1.9 and 3.1 m s^{-1}. With two exceptions (21 February 2006 and 11 July 2006), these acquisitions are associated with low wind speeds. The acquisitions listed in the third example with poor contrast between land and water (*'p'*, Table 1) coincides with high wind speeds of 3.2, 3.2, 3.6, 3.7 and 4.6 m s^{-1}.

For a 15 month period, wind speeds recorded at the day and night acquisition times were analyzed. Wind speeds were generally higher during the morning than during the evening (Figure 1.8). At the morning acquisition time, on 214 out of 430 days, the 2 m wind speed exceeds the 2.6 m s^{-1} Bragg scattering threshold, i.e. on only 50% of the days wind speeds were below the threshold. For evening overpasses, the Bragg scattering criterion is surpassed only during 18 out of 430 days, i.e., on 96% of the days wind speeds were below the threshold. The night time acquisitions therefore yield a much higher chance to obtain images where the water bodies are not affected by wind induced waves. The 10-day averages (morning acquisition in red, night acquisition in light blue) do not only show that wind speeds during the morning acquisitions are generally higher than those recorded at night, but also indicate a seasonal cycle.

During the dryer months from December to July, wind speeds are especially high during the morning acquisitions.

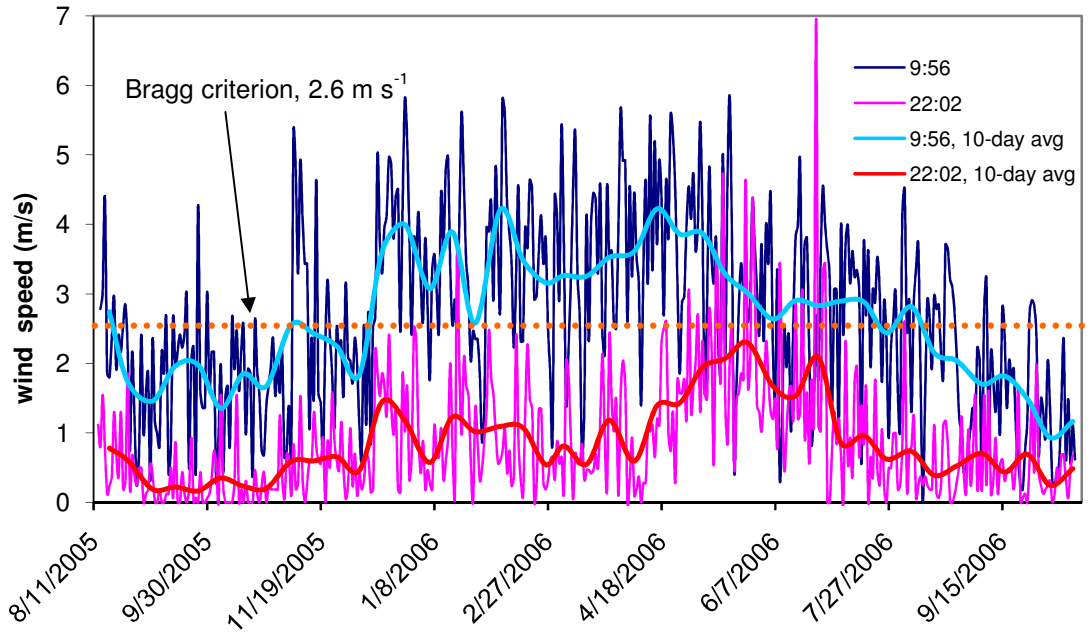

Figure 1.8: Measured wind speeds over the course of the year for morning (magenta, 10-day averages in red) and evening overpasses (dark blue, 10-day averages in light blue), and the wind speed Bragg criterion (orange).

1.6 Discussion

The surface extent of small reservoirs could be extracted from 21 of the 22 ENVISAT ASAR scenes used in this study, using the best band or band combination. The combination of both bands generally improved the classification result. For acquisition dates with image pairs consisting of an image with good and one with poor land-water-contrast or Bragg scattering effects, the classifi-

cation was performed on a single band. According to ESA's recommendation, image-mode VV polarized images should be used to map open water (ESA, 2007). Experience with a large number of ERS VV images, shows that for the purpose of monitoring small reservoirs, this is not the optimal choice. Instead, dual-polarized images are preferable for operational purposes. In general, HH images give the best results, but the HV images form a backup in case Bragg scattering occurs.

Stringent classification rules that allow simple and automated surface area extraction only produce results on a small number of images with excellent land-water contrast and coherent backscatter from within the water body. Due to the great variability and incoherence in the backscatter from water bodies, and in land-water contrast, stringent rules, however, fail quickly. With more flexible classification rules, such as the quasi-manual approach used here, good results were produced on all but one image. The fact that we have to manually identify the training area is comparable to purely visual techniques commonly employed in radar image analysis (Barber et al., 1996; Brakenridge et al., 1994; Henderson, 1995) and should not necessarily be considered a problem. Our quasi-manual approach differs from a fully manual, or visual, approach in that it is still based on backscatter statistics of the training areas and relationships among neighboring pixels, which allows us to set criteria that categorize "water-pixels" somewhat less subjectively, especially when Bragg scattering makes it difficult to visually identify all boundary pixels.

A comparison between reservoir sizes extracted from the ENVISAT ASAR scenes and the bathymetry based outlines (Figure 1.9) shows that the ENVISAT results (point markers) are generally lower than the bathymetry based surface

areas (line graphs). Figure 1.9 also shows that, as the reservoirs attain their maximum fill level, this difference increases, and eventually produces an almost constant offset during the period when the reservoirs are full. As the reservoir levels fall, the difference quickly diminishes. This increasing area differential with increasing fill levels, and the eventual offset at the maximum fill levels, is due to the development of wetland vegetation in the inflow part of the small reservoirs. When the fill levels approach the maximum capacity, distinct land-water boundaries diminish and the open water body often gradually changes into an extensive wetland at its inflow part. At these higher fill levels, GPS-based outlines obtained by walking around the reservoirs included these wetlands because they constitute, in reality, open water. As the bathymetric models partially depend on these GPS outlines, the offset introduced at the highest fill levels is an artifact from the data acquisition for the bathymetric models and, therefore, a direct result of the surveying. When the reservoir levels become lower again, this effect quickly diminishes together with the presence of wetlands, and the radar and bathymetry based area estimates converge. Taking into account this overestimation of the bathymetric data at full reservoir capacity as compared to ENVISAT classified reservoir areas, the overall classification results are acceptable.

The land-water separability is influenced by the vegetation context, and the natural variability of the water surface, often as a response to wind speed, which affects parts of, or the entire reservoir. To a large degree, the presence of tall vegetation around the reservoirs drastically improves the delineation of water bodies, as the low backscatter from the water surface itself stands in distinct contrast to the high backscatter from its edges, due to the high potential for double bounces off of the water and the vertical vegetation. Such double bounces

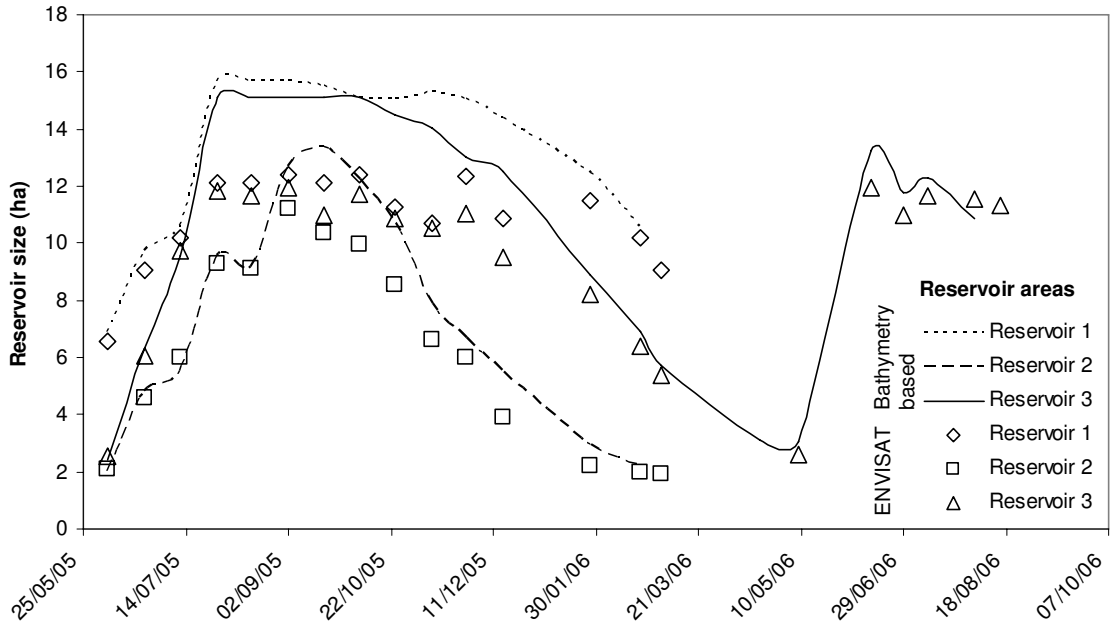

Figure 1.9: Comparison of reservoir sizes from ENVISAT classification (markers) with reservoir sizes from bathymetrical models (lines)

however only occur during the rainy season, and shortly thereafter, when the water levels are high and the vegetation is still lush. At the same time, exact delineation of the reservoirs can become difficult in the tail part at full capacity, when there is not a clear distinction between open water and wetland. During the dry season, when the water levels have decreased, the water bodies are surrounded by smoothly transgressing basin sides, which are mostly free of vegetation. Under these conditions, the land-water contrast is less distinct.

Wind was identified to affect the backscatter from water bodies. Images with very poor land-water contrast, and the acquisition from which the reservoirs could not be classified, coincided with high wind speeds and wind directions

which are propitious for Bragg scattering, whereas most images with excellent land-water contrast were acquired at low wind speeds and/or wind directions which are unfavorable for Bragg scattering. Choosing night time acquisitions clearly gives a higher chance of acquisitions at lower wind speeds. As is typical for most semi-arid areas, the onset of the rainy season, here from May-June, is a period with relatively high wind speeds. During this period, the chance to acquire scenes with clearly distinguishable small reservoirs diminishes.

A threshold value of 2.6 m s^{-1} at 2 m has been put forward as criterion for the occurrence of Bragg scatter. In the case of small reservoirs, we do indeed see that when winds are above this threshold, Bragg scatter occurs if the wave crests are perpendicular to the look direction. It should be noted that there were also occasions where minor wind gusts at low wind speed (1.0 m s^{-1}) in the look direction, caused Bragg scatter. In such cases the use of the dual polarization mode ENVISAT images is essential, because cross-polarized images are less affected.

1.7 Conclusion

The use of radar remote sensing as a tool for water resources monitoring is promising due to its ability to penetrate clouds, but the delineation of water bodies is difficult to automate. For time series analysis, an automated extraction of water bodies would be desirable but is not always possible due to the large variation in the radar backscatter from the water surface and to the changing ambient conditions. The quasi-manual method presented provides a good combination of computer objectivity and human classification skills.

The analysis of the radar image time series indicates that the land-water contrast, which is of greatest importance for the detection of water bodies, varies significantly with the seasons. Radar images acquired during the rainy season showed the best land-water contrast and were most easily classified. In the dry season, with smaller water bodies and lack of surrounding vegetation, their classification was more difficult as the land-water contrast diminishes. Toward, and throughout the dry season, the water detection on radar imagery is most difficult, as the land-water contrast suffers from the lack of vegetation context. Under such conditions, optical systems yield good results (Liebe et al., 2005), even on small water bodies, and independent of the surrounding vegetation and wind conditions, as long as cloud free images can be obtained. This leads to the important conclusion that optical and radar based methods can be seen as seasonally complementary for surface water detection, especially in semi-arid areas.

The backscatter signal of water bodies is significantly influenced by wind induced waves, and wave crest orientation. The analysis shows that Bragg scattering effects emerge at much lower wind speeds than ESA's wind speed threshold for Bragg scattering, which translates to wind speeds of 2.6 m s^{-1} (at 2 m height), however, the heavily affected acquisitions with poor land water contrast are all associated with wind speeds well above this threshold. The analysis of wind speed prevalence at the time of the morning and night time image acquisition show a distinct difference. Night time acquisitions are much less likely affected by wind than the morning acquisitions. For the delineation of water bodies, selecting night time acquisitions yield a significantly higher chance of obtaining radar images at wind speed conditions below the Bragg criterion. Although Bragg scattering was also observed below the 2.6 m s^{-1} threshold, Bragg pro-

ducing gusts are less likely during the night time acquisitions, when the atmosphere commonly has stabilized.

Overall, this study shows that regional to basin scale inventories of small inland water bodies are readily possible with ENVISAT ASAR images. In combination with regional area-volume equations (Cecchi, 2007; Liebe et al., 2005; Sawunyama et al., 2006, i.e.), basin-wide small reservoir storage volumes can be estimated, and the impact of further development can be assessed and monitored. With the ever improving digital elevation models it is foreseeable that area-volume equations can be determined adequately from these data, which will allow for regional and basin-wide small reservoir storage volume estimates at any given location. Further research could clarify whether ALOS PALSAR's L-Band data yields better land-water separation under the various wind conditions and seasonal changes in vegetation context, which would allow extracting small reservoirs and other inland water bodies at a higher degree of automation.

REFERENCES

Barber, D., Hochheim, K., Dixon, R., Mosscrop, D., McMullan, M., 1996. The role of earth observation technology in flood mapping: A Manitoba Case study. Canadian Journal of Remote Sensing 22 (1), 137–143.

Brakenridge, G., Knox, J., Paylor II, E., Magiligan, F., 1994. Radar Remote Sensing Aids Study of the Great Flood of 1993. EOS 75 (45), 521–530.

Brivio, P. A., Colombo, R., Maggi, M., Tomasoni, R., 2002. of remote sensing data and GIS for accurate mapping of flooded areas. International Journal of Remote Sensing 23 (3), 429–441.

Cecchi, P. (Ed.), 2007. L'eau en partage: les petits barrages de la Côte d'Ivoire. Vol. Collection Latitudes 23. IRD Edition, Paris.

ESA, 2005. Bragg scattering. `http://earth.esa.int/applications/data_util/SARDOCS/spaceborne/Radar_Courses/Radar_Course_II/Bragg_scattering.htm`.

ESA, 2007. ASAR Product Handbook. `http://envisat.esa.int/handbooks/asar/CNTR1-1-6.htm`.

Faulkner, J. W., Steenhuis, T., De Giesen, N. V., Andreini, M., Liebe, J. R., 2008. Water use and productivity of two small reservoir irrigation schemes in Ghana's Upper East Region. Irrigation and Drainage 57 (2), 151–163.

Gardini, B., Graf, G., Ratier, G., 1995. The Instruments on ENVISAT. Acta Astronautica 37, 301–311.

Henderson, F. M., 1995. Environmental Factors and the Detection of Open Surface Water Areas with X-Band Radar Imagery. International Journal of Remote Sensing 16 (13), 2423–2437.

Henderson, F. M., Lewis, A. J. (Eds.), 1998. Principles and applications of imaging radar, 3rd Edition. Vol. 2. John Wiley and Sons, New York.

Henry, J. B., Chastanet, P., Fellah, K., Desnos, Y. L., 2006. Envisat multi-polarized ASAR data for flood mapping. International Journal of Remote Sensing 27 (9-10), 1921–1929.

Heremans, R., Willekens, A., Borghys, D., Verbeeck, B., Valckenborgh, J., Acheroy, M., Perneel, C., 2003. Automatic detection of flooded areas on ENVISAT/ASAR images using an object-oriented classification technique and an active contour algorithm. In: 1st Int. Conf. on Recent Advances in Space Technologies. Istanbul, Turkey.

Horritt, M. S., Mason, D. C., Luckman, A. J., 2001. Flood boundary delineation from Synthetic Aperture Radar imagery using a statistical active contour model. International Journal of Remote Sensing 22 (13), 2489–2507.

Kranjac-Berisajevic, G., Bayorbor, T. B., Abdulai, A. S., Obeng, F., 1998. Rethinking Natural Resource Degradation In Semi-Arid Sub-Saharan Africa: The Case of Semi-Arid Ghana.

Liebe, J., Andreini, M., van de Giesen, N., Steenhuis, T., 2007. The Small Reservoirs Project: Research to Improve Water Availability and Economic Development in Rural Semi-arid Areas. In: Kittisou, M., Ndulo, M., Nagel, M., Grieco, M. (Eds.), The Hydropolitics of Africa: A Contemporary Challenge. Cambridge Scholars Publishing, Newcastle, pp. 325–332.

Liebe, J., van de Giesen, N., Andreini, M., 2005. Estimation of small reservoir storage capacities in a semi-arid environment - A case study in the Upper East Region of Ghana. Physics and Chemistry of the Earth 30 (6-7), 448–454.

Nico, G., Pappalepore, M., Pasquariello, G., Refice, A., Samarelli, S., 2000. Comparison of SAR amplitude vs. coherence flood detection methods - a GIS application. International Journal of Remote Sensing 21 (8), 1619–1631.

Sawunyama, T., Senzanje, A., Mhizha, A., 2006. Estimation of small reservoir storage capacities in Limpopo River Basin using geographical information systems (GIS) and remotely sensed surface areas: Case of Mzingwane catchment. Physics and Chemistry of the Earth 31 (15-16), 935–943.

Sutton, O. G., 1934. Wind Structure and Evaporation in a Turbulent Atmosphere. Proceedings of the Royal Society of London. Series A, Containing Papers of a Mathematical and Physical Character 146 (858), 701–722.

Valenzuela, G. R., 1978. Theories for the interaction of electromagnetic and oceanic waves: A review. Boundary Layer Meteorology 13, 61–85.

van de Giesen, N., 2001. Characterization of West African shallow flood plains with L- and C-Band radar. In: Owe, M., Brubaker, K. (Eds.), Remote Sensing and Hydrology 2000. Vol. 267. IAHS Publication, pp. 365–367.

Van der Sanden, J. J., Thomas, S. J., 2004. Application Potential of RADARSAT-2. Supplement One. `http://www.radarsat2.info/sartrek/2005/jun/RSAT2_APPS_2004_PDF_Final.pdf`.

Windmeijer, P. N., Andriesse, W. (Eds.), 1993. Inland Valleys in West Africa: An Agro-Ecological Characterization of Rice-Growing Environments. Vol. 52 of ILRI Publication. International Institute for Land Reclamation and improvement, Wageningen.

Xu, C. Y., Prince, J. L., 1998. Snakes, shapes, and gradient vector flow. IEEE Transactions on Image Processing 7 (3), 359–369.

CHAPTER 2

DETERMINING WATERSHED RESPONSE IN DATA POOR ENVIRONMENTS WITH REMOTELY SENSED SMALL RESERVOIRS AS RUNOFF GAUGES

2.1 Introduction

In semi-arid Africa, governments and communities have difficulty managing water supplies due to hydroclimatic variability and ever increasing population pressure. Uncertainty arises due to a lack of information, poor understanding of hydrological processes, and absence of suitable models for these environments. Especially in international river basins, this uncertainty leads to unnecessary tension since equitable sharing and utilization of water resources is difficult in the absence of informed planning and coordinated development.

Although more and more data become available on a regional basis with the World Hydrological Cycle Observing Systems (WHYCOS) framework (WMO, 2005), watershed interventions, such as the construction of small and intermediate sized reservoirs, cannot be studied using regional water balances. Small reservoirs can reduce the reliability of water supplies at the local level, but may reduce the overall yield from a watershed. In the Volta basin, the construction of these small reservoirs is hotly debated because they may reduce the flow to Lake Volta that stores water for the major hydroelectric generating plant in Ghana.

In order to improve our understanding of the impact of small reservoirs on downstream flows, these reservoirs themselves can be used as runoff gauges by remotely measuring their surface areas and converting these measurements

to volume estimates with the regional area-volume relationship developed by Liebe et al. (2005). Several studies have been published on mapping or monitoring reservoir surface areas with satellite images of small reservoirs (White, 1978; McFeeters, 1996; Frazier and Page, 2000). Mialhe et al. (2008) estimated small reservoir storage volumes from Landsat images in India. While Meigh (1995) quantified the impact of small farm reservoirs in Botswana on larger reservoirs downstream using field data, none of the other studies were able to quantify their impact on the downstream water resources, due to the lack of suitable hydrological models, and none have used the reservoirs as runoff gauges. Satellite images for mapping the small reservoirs can be obtained from optical (i.e. Landsat, Spot, Aster, ISS, etc.) or radar satellite systems (ENVISAT, ERS, Radarsat, etc.). While optical systems are easier to process, surface observations are often hindered by clouds. Radar remote sensing is not affected by cloud cover and has an advantage over optical remote sensing platforms in acquiring time series under frequently cloudy conditions. The detection of water bodies on radar images can be affected by wind-induced waves, and vegetation context (Liebe et al., 2009).

The main objective of this research is to show how in a data scarce environment, such as Ghana, remote sensing of existing reservoirs can be used to characterize runoff processes. In particular, we will test if existing reservoirs can be used as runoff gauges by remotely sensing their size.

2.2 Study Area and Hydrology

The Upper East Region of Ghana, and northern Togo (Figure 2.1) are characterized by a mono-modal rain season from July to September with almost 1,000 mm of average annual rainfall, and 2,050 mm of average annual potential evaporation (Kranjac-Berisajevic et al., 1998). Small reservoirs are typically located on the head of larger watersheds. Overland flow commonly plays a secondary role in these regions, as infiltration rates are generally high and storm durations are short (Masiyandima et al., 2003; van de Giesen et al., 2000, 2005). The quick response to rainfall is mainly due to interflow. Distinct inflow channels into the reservoirs are usually absent. Runoff generation in semi-arid areas typically follows a distinct pattern. The first rains at the start of the wet season wet up the soil that is dried out after the extended dry season. These rains hardly produce any runoff. Only after the soils are above field capacity does water flow from the watershed to the reservoir. The contributing area increases with the size of the storms. In the study region, small reservoir storage volumes can be estimated as a function of their surface areas (Liebe et al., 2005) with

$$V = 0.00851 \; {A_{Res}}^{1.4367} \tag{2.1}$$

where V is the volume of a reservoir [m^3], and A_{Res} is its area [m^2]. Since the sides of these reservoirs have gentle slopes, minor changes in depth result in relatively large surface area changes.

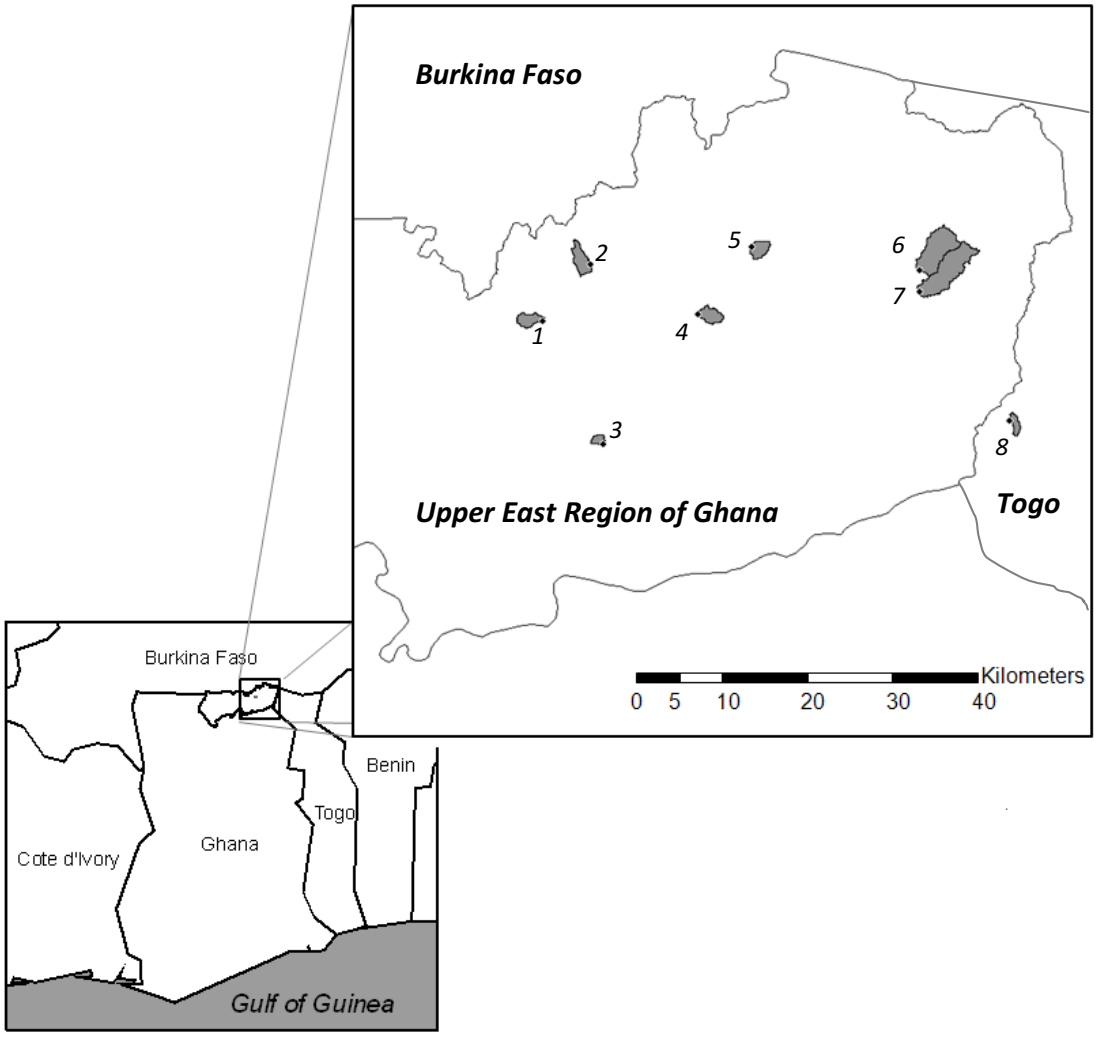

Figure 2.1: Location of eight reservoirs (dots) and the associated watersheds (shaded) in the eastern part of the Upper East Region of Ghana, and Togo.

2.3 Materials and Methods

The basic assumption behind this research is that small reservoirs can be used as runoff gauges observed with satellites. Reservoir surface areas were extracted from twelve ENVISAT ASAR images from May 21, 2005 to August 15, 2005, and

from June 13, 2006 to August 15, 2006, covering the end of the dry season, the onset of the rainy season, as well as the early rainy season. ENVISAT ASAR is a C-band radar, which provides images at a spatial resolution of 30 m (Gardini et al., 1995). The images used in this study were acquired in dual polarization mode (HV / HH), which also has been found useful in flood studies by Henry et al. (2006). The reservoir surface areas were extracted using a quasi-manual classification approach, which is based on training areas digitized inside the water bodies (Liebe et al., 2009). The watershed of each reservoir was delineated using SRTM V3 elevation data (Jarvis et al., 2006), which have a spatial resolution of 90 m, and a relative vertical accuracy of better than 10 m. After performing a pit-removal procedure, the stream network was extracted, and the reservoirs' watershed boundaries were determined with Idrisi software by choosing the dam wall as the seed point. The reservoir surface is included in the total watershed area, $A_{(WS+Res)}$. For the hydrological modeling, although the overall effect may be very small, a reduced watershed area, A_{WS}, is used, which is obtained by subtracting the time dependent reservoir area, A_{Res}, from the total watershed area $A_{(WS+Res)}$ (*i.e.* A_{WS}=$A_{(WS+Res)}$-A_{Res}).

Rainfall estimates were obtained from the Famine Early Warning Systems Network (FEWS NET). The FEWS NET rainfall estimates are a computer-generated product with a horizontal resolution of 10 km (Xie and Arkin, 1997) based on Meteosat infrared data, rain gauge reports, and microwave satellite observations. Monthly means of daily evaporation rates were obtained from the Meteorological Station in Navrongo, Ghana (10°53'1" N, 1°5'4" W, Table 2.1), and were generally in the range 4.4-6.2 mm day^{-1} during the period of study from May to August. By combining reservoir surface areas with the known relationship between reservoir volume and surface area (Equation 2.1), changes in

reservoir storage can be calculated and the discharge from the watershed to the reservoirs can be determined. In this region, thick clay layers ($K_{sat} \approx 0.1$ mm day^{-1}, Rawls et al. 1983) are typically found in the subsoil (Edmonds, 1956). Accordingly, percolation rates were set at 3 mm month^{-1}.

Table 2.1: Penman reference evaporation rates from long term averages (1961-1990) for the Meteorological Station Navrongo (10°53'1" N, 1°5'4" W, 201.3 m asl)

Month	Jan.	Feb.	Mar	Apr.	May	Jun.	Jul.	Aug.	Sep.	Oct.	Nov.	Dec.
Pen ET_0 [mm day^{-1}]	6.0	6.7	6.9	6.7	6.2	5.3	4.7	4.4	4.6	5.2	5.3	5.4

(after Kranjac-Berisajevic et al., 1998)

2.4 Observed Runoff Calculations

To determine the hydrological watershed response, reservoir storage increase through direct rainfall on the reservoirs has to be subtracted. Since the remotely sensed areas are only available at intervals of approximately 14 days, and not necessarily on days when it rained, the reservoir area changes occurring between image acquisition dates were estimated. When reservoirs become larger, the reservoir areas are assumed to increase on dates with significant rainfall, while on the dry days, the reservoir areas were assumed to have remained the same:

For $A_{(Res)} > A_{(Res-n)}$ and $\tau\text{-}n \leq t \leq \tau$

$$A_{(Res)_t} = \begin{cases} A_{(Res\ t-1)} + \frac{N}{n}\left(A_{(Res\ \tau)} - A_{(Res\ \tau-n)}\right), & \text{for } \textit{'wet days'} \\ A_{(Res\ t-1)}, & \text{for } \textit{'dry days'} \end{cases} \tag{2.2}$$

where *n* represents the number of days between two consecutive image acquisitions taken at time τ and $\tau - n$, *N* is the number of wet days in this time period, and A_{Res} is the remotely sensed reservoir area. Based on Acheampong's (1988) definition of a *'wet'* month, a day is considered *'wet'* when the rainfall in the ten preceding days exceeds 34 mm, and rainfall exceeds potential evaporation on that day, i.e.

$$'wet\ day'_t = \sum_{i=t}^{t-10} P_i > 34 \text{ mm} \bigwedge P_t - E_{pot_t} > 0 \text{ mm} \tag{2.3}$$

where on a day *t*, P_t is the depth of precipitation and E_{pot_t} is potential evaporation. When the reservoir decreases in size, a different interpolation procedure is followed with the reservoir area decreasing on dry days and remaining constant on *'wet'* days, i.e., for $A_{Res\ \tau} < A_{Res\ \tau-n}$ and $\tau\text{-}n \leq t \leq \tau$

$$A_{Res_t} = \begin{cases} A_{Res\ t-1}, & \text{for } \textit{'wet days'} \\ A_{Res\ t-1} - \frac{n-N}{n}\left(A_{Res\ \tau-n} - A_{Res\ \tau}\right), & \text{for } \textit{'dry days'} \end{cases} \tag{2.4}$$

The volume of water in the reservoir increases due to quickflow which is interflow from the watershed and precipitation on the reservoir. The volume decreases due to evaporation from the reservoir. The change in reservoir volume *V* between two subsequent images at time $\tau - n$ and τ, equals

$$\Delta V_\tau = V_\tau - V_{\tau-n} \tag{2.5}$$

where *V* is the total volume of the reservoir at the time indicated by the subscript. The increase in the volume of water due to inflow from the watershed, ΔV_{WS}, can be calculated by taking the change of volume, ΔV_τ, estimated from the areas taken from the satellite imagery and then subtracting the net change due to evaporation and rainfall of the reservoir itself, ΔV_{Res}:

$$\Delta V_{WS} = \Delta V_\tau - \Delta V_{Res} \tag{2.6}$$

ΔV_{Res} [L^3] can be calculated as:

$$\Delta V_{Res} = \frac{A_{Res\ \tau} - A_{Res\ \tau-n}}{2} \left[\sum_{\tau-1}^{\tau} (P_t - E_{pot\ t}) - K_{sat} \Delta t \right] \quad (2.7)$$

where E_{pot} [L/T] is the potential evaporation, P [L/T] is the rainfall and K_{sat} [L/T] is the leakage from the reservoir.

Figure 2.2 shows the procedure of calculating ΔV_τ from ΔV_{Res} and ΔV_{WS}. Circles indicate the total reservoir storage, V, estimated from ENVISAT ASAR images. The storage volume on the first date represents the amount of water that remained in the reservoir after the end of the dry season, and serves as a reference level for storage change. The part of the reservoir storage change, ΔV_{Res} due to rainfall and evaporation on the reservoir is calculated with Equation 2.7. The volume entering the reservoir from interflow, ΔV_{WS}, can be calculated by taking the difference with Equation 2.6. The contribution of the watershed to the reservoir storage volume, ΔV_{WS}, is used to estimate parameters for the rainfall-runoff method described below.

2.5 Runoff Model

Data availability in Ghana is relatively poor. Fully distributed hydrological models are, therefore, not appropriate. Instead, we have to look for models with only a few parameters, which capture the main hydrological characteristics of the area. It is especially important that the model predicts the increasing fraction of rainfall that reaches the reservoir as the storm progresses (Masiyandima et al., 2003; Liu et al., 2008). One of the methods that works well in tropical climates is the Thornthwaite-Mather (1955) procedure which has been successfully applied throughout the humid tropical area (Peranginangin et al., 2004), and in

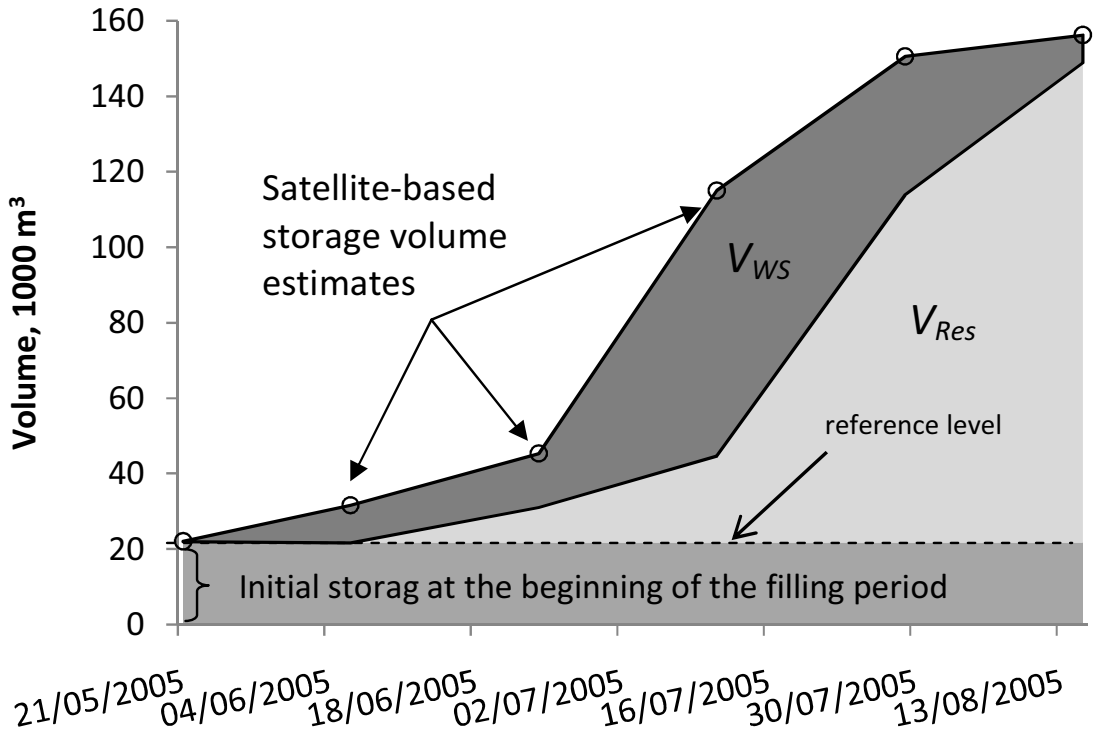

Figure 2.2: Evolution of the water volume in Reservoir 2 during the 2005 rainy season.

Circles depict satellite based reservoir storage volume estimates. V_{Res} represents the water that has fallen directly on the reservoir minus the evaporation from the reservoir and V_{WS} is volume of water due to inflow from the watershed.

semi-arid areas (Norman and Walter, 1993; Taylor et al., 2006). It is modified to predict the increasing fraction of the percolation water reaching the reservoir with increasing rainfall amounts. The rainfall-runoff model is developed as follows. A portion of the soils around the reservoirs are sandy and have a high infiltration rate. The remaining soils are lateritic with smaller conductivity values than the sand but high enough to allow the rainfall to infiltrate. Water is transported in the sandy soils as subsurface flow to the reservoir. After the sandy soils have been sufficiently wetted to a storage level in the root zone,

called S_{max}, any excess rainfall percolates down and flows to the reservoir in a relatively short time because of the high conductivity of the soil and the slope of impermeable layer towards the reservoir. The amount of water needed to wet up the entire profile before runoff occurs varies. Hence the area that contributes interflow increases with increasing rainfall amounts.

The water balance for the root zone can be written as:

$$S_t = S_{t-\Delta t} + (P - E_{act} - P^*)\Delta t \tag{2.8}$$

where P is precipitation [L/T], E_{act} is actual evaporation [L/T], and $S_{t-\Delta t}$ is the previous time step storage in the root zone per unit area [L]. P^* is the effective rainfall [L/T], i.e. the amount of rainfall that exceeds the soil's field capacity and is available for percolation. Δt is the time step, and S_t [L] is the amount of water stored in the root zone at time t. For simplicity we do not use a subscript here other than for the storage in the root zone.

During wet periods, when rainfall exceeds potential evaporation (i.e., $P > E_{pot}$), actual evaporation, E_{act}, is equal to potential evaporation, E_{pot}. Percolation occurs due to effective rainfall, P^*, when the soil moisture content is above field capacity, e.g.

$$P^* = S_{t-\Delta t} - S_{max} + (P - E_{pot})\Delta t \tag{2.9}$$

The soil always drains to field capacity within the time period, thus we find for the storage in the soil that

$$S_t = S_{max} \tag{2.10}$$

where the available soil storage capacity, S_{max} [L], is defined as the difference

between the amount of water stored in root zone at wilting point and at field capacity, i.e.

$$S_{max} = d_{rz}(\theta_{fc} - \theta_{wp}) \tag{2.11}$$

where d_{rz} is the root zone depth [L], θ_{fc} is the moisture content at field capacity, and θ_{wp} is the moisture content at wilting point. Conversely, when evaporation exceeds rainfall (i.e., $P < E_{pot}$), the Thornthwaite and Mather procedure is used to calculate the actual evaporation E_{act} (Steenhuis and van der Molen, 1986). In this method, E_{act} decreases linearly with moisture content:

$$E_{act} = E_{pot}\left(\frac{S_t}{S_{max}}\right) \tag{2.12}$$

When $P < E_{pot}$, the storage in the root zone (above the wilting point) can be written, based on Equation 2.8, as:

$$S_t = S_{t-\Delta t}\left[exp\left(\frac{(P - E_{pot})\Delta t}{S_{max}}\right)\right] \text{ when } P < E_{pot} \tag{2.13}$$

Percolation through the root zone flows either to the deep groundwater or towards the reservoirs as quick or interflow. Quickflow, Q_f, is the amount of effective rainfall (i.e., percolation) that reaches the reservoir. This leads to an increase in reservoir volume of ΔV_{WS}. The fraction of the percolation that recharges the reservoir, Q_f, increases with rainfall. Conceptually, as discussed above, we can explain this as an increase in contributing area to the reservoir, which becomes larger when rainfall amounts increase (Liu et al., 2008). This relationship between contributing area and effective rainfall amounts is not known. Such a relationship should have the property that the contributing area is zero when rainfall just wets up the soil to field capacity, and should be equal to 1 when rainfall approaches infinity. One such an expression is:

$$Q_f = P^* \left(1 - exp\left(-a \times P^*\right)\right) \tag{2.14}$$

where '*a*' is a constant, which is an indicator how fast the contributing area is increasing. Figure 2.3 depicts the production of Q_f as a function of P^* and different '*a*' values. As shown in Steenhuis et al. (1995), we can differentiate Equation 2.14 with respect to P^* to obtain the contributing area A_f, i.e.

$$A_f = 1 + (a \times P^* - 1)\, exp(-a \times P^*) \tag{2.15}$$

We can see that Equation 2.15 has the required property of A_f =0 when P^* =0, and A_f = 1 when $P^* \rightarrow \infty$.

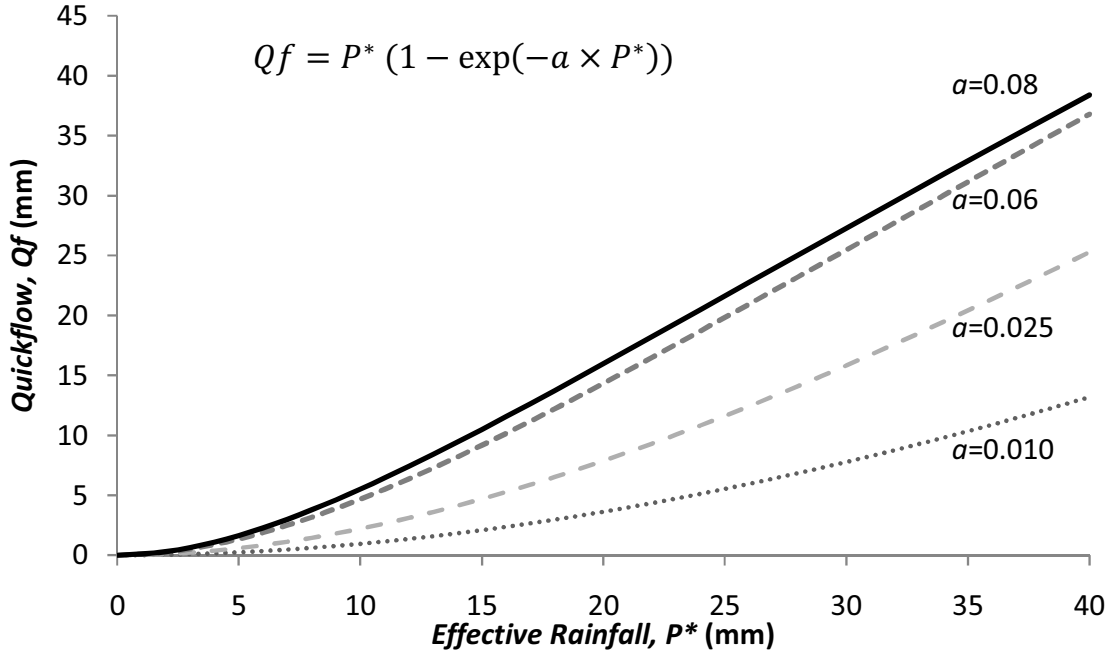

Figure 2.3: Quickflow, Q_f, as a function of the effective rainfall, P^*, for different watershed factors '*a*' (Equation 2.14)

2.5.1 Calibration and Validation

The records for the eight reservoirs are divided into two years. The parameters S_{max} and '*a*' are calibrated using the 2005 data, and then used in 2006 for validation. In calibration, the S_{max} determines mainly the time of the first watershed contribution to the reservoir, while '*a*' is related to the total amount of percolation that reaches the reservoir. Figure 2.4 shows how the parameters are

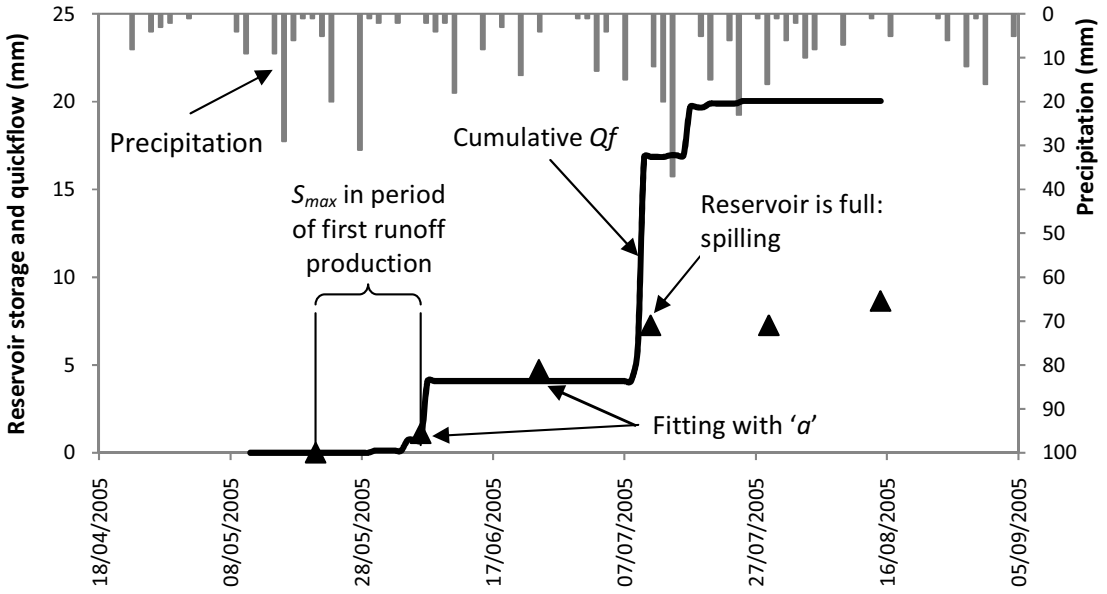

Figure 2.4: Example of Reservoir 6, 2005, for the calculations to determine the maximum storage of the root zone, S_{max}, and the watershed parameter, '*a*', that determines the rate that the saturated areas are expanding.

S_{max} is determined in the period of first observed runoff. The predicted cumulative quickflow, Q_f (bold line) is fitted with Equation 2.14 to the observed quickflow volumes (triangles) using the parameter '*a*' as a calibration factor.

obtained. S_{max} is determined in the time range when the reservoir rises first, i.e. when the first watershed response is observed in the reservoir. Initially, two S_{max} values are determined with the Thornthwaite-Mather procedure. The

maximum S_{max} value is determined assuming that the first percolation occurs on the date that the first rise in the reservoir was observed with the satellite image, and the minimum S_{max} values were calculated assuming that the rise occurred at the preceding satellite image acquisition date. In the Thornthwaite-Mather model the mean S_{max} value was used.

The shape factor value, '*a*', is obtained by visually fitting predicted reservoir inflow with Equation 2.14 to the observed inflow based on volume increases determined with satellite images. The method does not apply once the reservoir is full, because inflows are then routed through the reservoirs over their spillways and do not result in an increase in storage.

2.6 Results

2.6.1 Reservoir and watershed sizes

The results of the reservoir surface area classification obtained from the radar image analysis are listed in Table 2.2. Reservoir storage volume estimates were made using Equation 2.1 and the observed reservoir surface areas. This time series of reservoir storage volumes is the basis for the calibration of the runoff model. The watersheds extracted from the SRTM DEM, including the reservoirs, range from 144 to 1,829 ha (Table 2.3).

Table 2.2: Reservoir surface areas [ha] classified from ENVISAT ASAR images.

Date	Reservoir surface areas [ha]							
	1	2	3	4	5	6	7	8
5/21/2005	5.5	2.9	3.5	6.6	6.6	9.4	4.3	3.6
6/6/2005	5.8	3.7	3.1	7.8	3.3	10.2	25.0	4.1
6/24/2005	6.1	4.7	3.7	10.0	12.6	12.9	26.3	4.8
7/11/2005	8.2	9.0	4.8	9.8	13.4	14.6	28.2	8.2
7/29/2005	8.8	10.9	7.2	10.2	17.0	14.1	29.5	8.6
8/15/2005	8.3	11.2	5.6	12.9	17.6	15.0	29.4	8.8
...	...	...	...	...	...	...	...	...
6/13/2006	4.9	2.2	5.4	9.9	6.0	4.0	1.8	4.1
6/29/2006	5.1	2.3	5.3	9.9	6.6	3.9	2.4	4.3
7/11/2006	5.0	2.4	5.5	10.1	7.0	4.1	1.8	4.6
7/30/2006	8.0	5.9	7.2	13.7	10.9	12.6	21.3	7.6
8/3/2006	8.5	6.1	5.5	14.4	11.5	13.1	21.6	7.8
8/15/2006	8.7	7.4	8.9	14.8	14.1	15.1	27.0	8.6

The location of the reservoirs is given in Figure 2.1

Table 2.3: Measured watershed area and calibrated root zone storage, S_{max} and watershed contributing factor, '*a*'.

Reservoir	1	2	3	4	5	6	7	8
Watershed area [ha]	822	518	144	403	357	1549	1829	194
S_{max} mean [mm]	45	42.5	45	42.5	32.5	25	45	37.5
S_{max} low/high [mm]	35/55	35/50	40/50	40/45	20/45	15/35	35/55	20/55
'*a*' [-]	0.010	0.025	0.063	0.060	0.080	0.013	0.020	0.035

The location of the reservoirs is given in Figure 2.1

2.6.2 Rainfall Characteristics

In 2005, the rainy season can be segmented into three to five wet periods with distinct dry spells in between. In 2006, there are only three wet periods, which were separated by only short dry spells. Figure 2.5 shows the results of the *'wet*

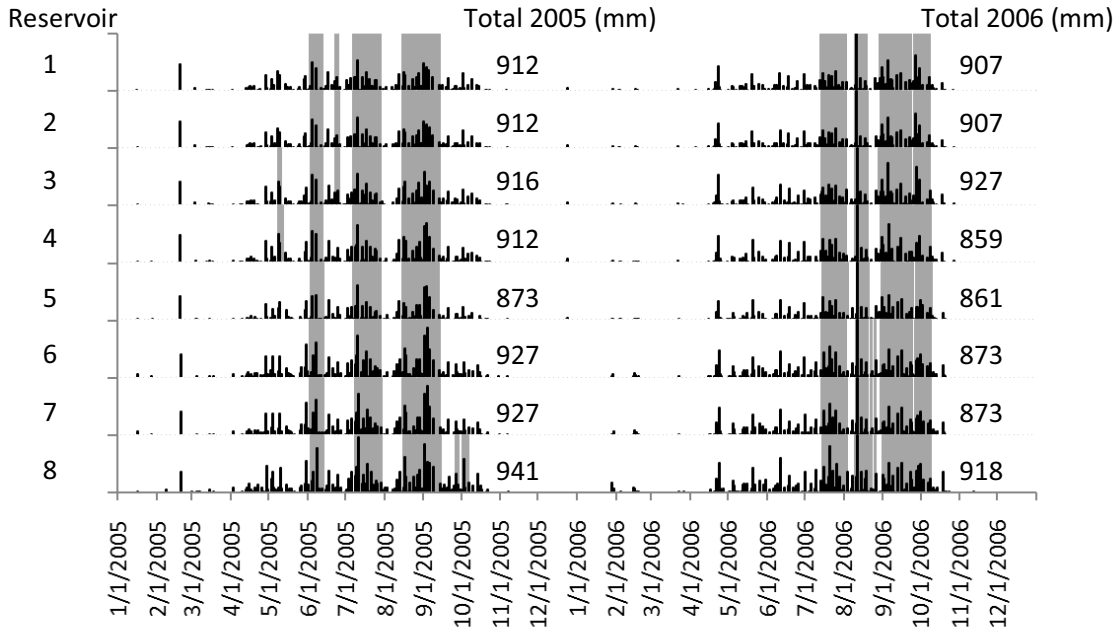

Figure 2.5: Normalized precipitation patterns (black bars), scaled from 0 to 1 with respect to the maximum rainfall event observed within the two years (min 45 mm, max 66 mm, avg. 56.6 mm), and occurrence of *'wet days'* (gray) according to Equation 2.2 for the 8 reservoirs in 2005 and 2006.

day' analysis for all watersheds, which is taken here as an indicator of the rainy season. Precipitation is scaled from 0 to 1 with respect to the maximum rainfall observed within the two years. Although the rainfall in 2006 was, on average, only 3% below the rainfall in 2005, the rainfall patterns were distinctly different. Overall, the 2006 rainy season was shorter and occurred later than the rainy season in 2005. In 2006 there were 67 wet days. Fifty nine percent of rain fell

on those days. In 2005, on average, 51% of the total precipitation fell on 63 wet days.

2.6.3 Rainfall-Runoff Relationships

For each watershed, the calibrated minimum, maximum and mean values S_{max} and the shape factor value '*a*' are reported in Table 2.3. The watersheds' mean S_{max} values range from 25 to 45 mm, and the '*a*' values range from 0.01 to 0.08. It is remarkable that for these watersheds that are spread over the northern part of Ghana and western part of Togo, similar S_{max} and '*a*' values can describe how and when the reservoirs fill up. A detailed example of the runoff model for one of the watersheds is shown in Figure 2.6. There are four rainfall events in which the soil is predicted to reach field capacity and quickflow occurs. To check how well these predictions are, the quickflows are accumulated and compared to the observed volumetric storage contribution from the watershed, ΔV_{WS}, which were calculated from the remotely sensed reservoir areas with Equation 2.6. The reservoir volume ΔV_{WS} is given as an equivalent watershed depth (i.e., the reservoir volume divided by the watershed area). In 2005, the first inflow into the reservoir occurred in early June. Both the increase in volume (obtained from the satellite image and indicated by the triangles) and the simulated results (solid line) agreed. This is not surprising since the year 2005 was used for calibration. In 2006, the same parameter set was used to predict the reservoir response. For this year, the first predicted inflow was in mid July which was in accordance with the observed increase in reservoir storage from the satellite image. The remaining two storms were predicted well with the last storm causing the reservoir to overflow. Also the filling pattern agreed well.

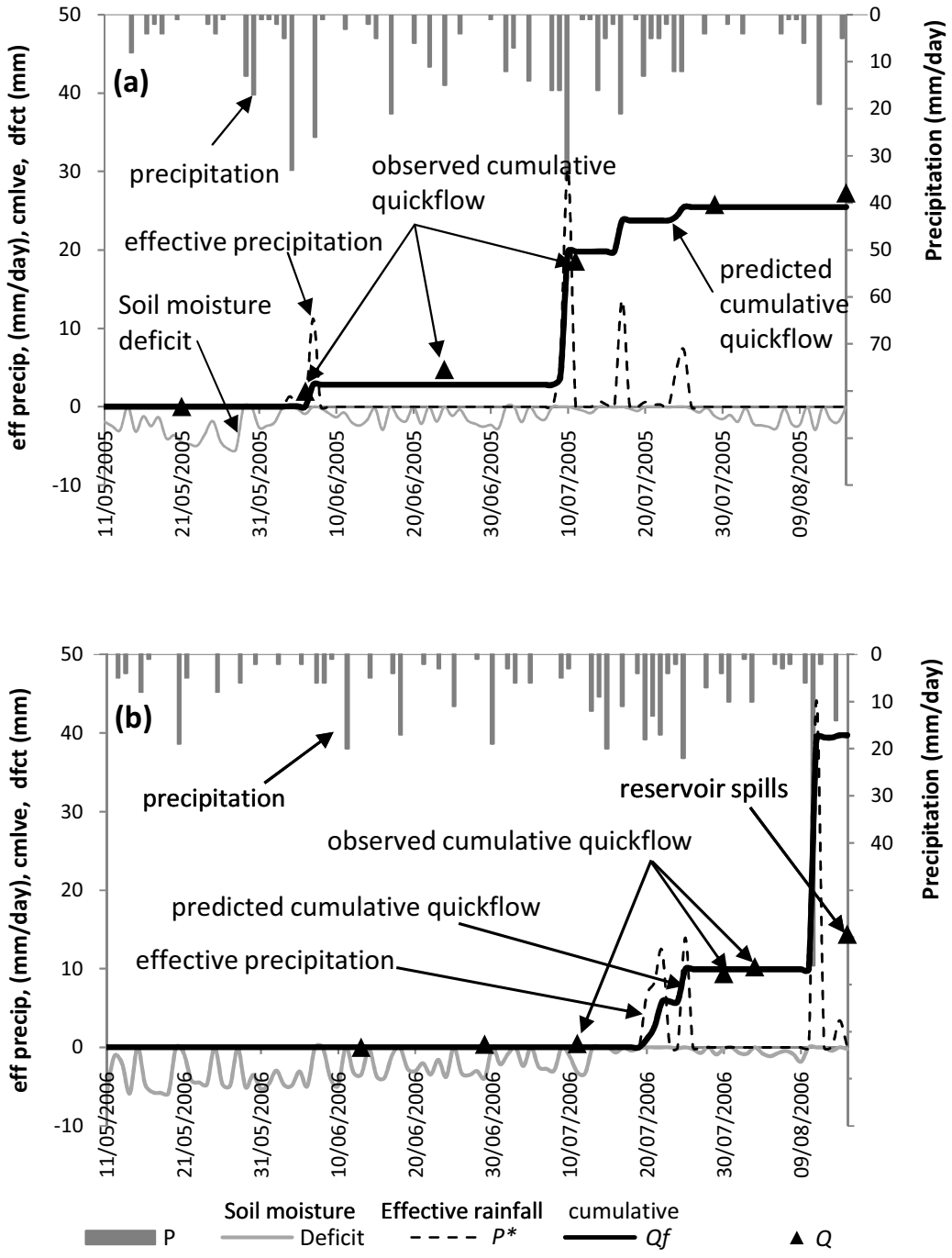

Figure 2.6: Observed (triangles) and predicted (bold lines) cumulative quick flow (Equation 2.14), moisture deficit (gray line, defined as $E_{act} - E_{pot}$), effective rainfall (P^*), and precipitation (black bars) for reservoir 2. (a) Calibrated model in 2005 (S_{max} =42.5 mm; '*a*' = 0.025) and (b) Validated model in 2006.

The ability of the model to predict reservoir storages for the other watersheds was also satisfactory. Figure 2.7, compares the observed reservoir volumes with the predicted cumulative quick flow Q_f) for the eight watersheds. In both years, the reservoirs were spilling water in August and therefore images taken on August 15, 2005, and August 15, 2006 were omitted from the analysis, because the reservoir area becomes constant and cannot be used as a runoff gauge anymore. The data obtained from the satellite images and the volumes predicted by the model were well correlated with an overall r^2 of 0.83 in 2005 and an r^2 of 0.92 in 2006.

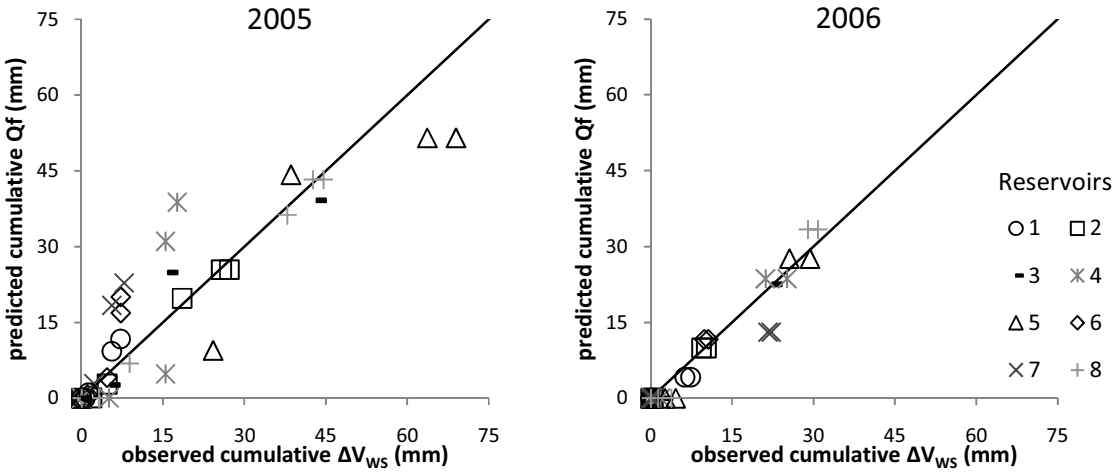

Figure 2.7: Observed and predicted cumulative runoff in the calibration year 2005 (left, r^2=0.83) and the validation year 2006 (right, r^2=0.92).

2.7 Discussion

Our results show that remotely sensed reservoirs can be used as a runoff gauges to better understand the hydrology of the landscape. Figure 2.6 shows that af-

ter the dry season, at the time that quick flow starts, the Thornthwaite-Mather procedure can be used with a similar storage value for most of Northern Ghana and Northwestern Togo. The portion of the effective rainfall (i.e., amount of rain after the soil is at field capacity) that becomes quick flow increases with rainfall amount because the area that contributes quick flow to the reservoir becomes larger as the storm progresses. In previous analyses such as by Taylor et al. (2006) it was assumed that the contributing area was constant. It is of interest to examine the rainfall pattern that caused the reservoirs to fill up. In 2005, a total of 211 mm of rain fell prior to June 4, when the reservoir started to fill. In 2006, 312 mm of rain fell prior to the first modeled runoff on July 20. Clearly, total rainfall is not the parameter that determines when the reservoir starts to fill. The model helps us to understand what kind of rainfall pattern starts to fill the reservoir. In the model, quick flow is generated when the soil is at field capacity. This occurs when the precipitation is in excess of evaporation over a period that is more than the amount of water needed to bring the soil to field capacity. Thus, any time when $P - E_{pot}$ over a period is more than S_{max}, the reservoir will start filling up. In reality, the filling-up will occur earlier, because the soil is not completely dry and the evaporation is not at the potential rate. Despite this, we can see that only during wet periods, when the rainfall is in excess of potential evaporation by an amount in the order 2-4 cm, the reservoirs will start to fill up. In 2006 (Figure 2.5, Figure 2.6 b) such a period did not occur until the middle of July. The watershed model developed in this paper can be used to estimate the impact of small reservoirs on downstream flows. For each reservoir and year, Figure 2.8 depicts the fraction of quickflow Q_f that is captured in the reservoirs, the fraction of quickflow Q_f that spills, and the amount of deep groundwater recharge (P^*-Q_f). The reservoirs are sorted by decreasing

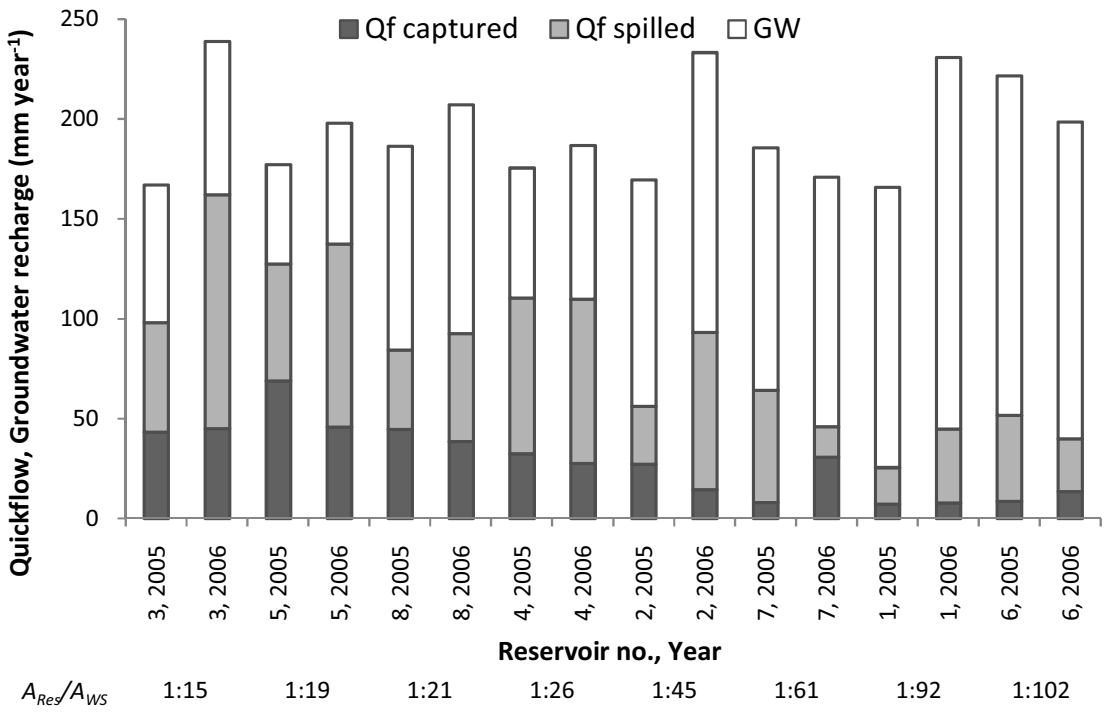

Figure 2.8: Impact of reservoirs on water resources (quickflow, Q_f, and ground water, *GW*).

A_{Res}/A_{WS} ratios from left to right. Despite the inter-annual variations, the figure shows the decreasing impact of reservoirs on the total quickflow Q_f and percolation with decreasing A_{Res}/A_{WS} ratios. This result is intuitive. Not included in the analysis is groundwater recharge through seepage from reservoirs, and inefficiencies in the small scale irrigation systems (Faulkner et al., 2008), which remain available as groundwater downstream. The effective impact of small reservoirs on available water resources is, therefore, likely to be smaller than the captured Q_f fraction shown in Figure 2.8.

2.8 Conclusion

In ungauged basins, using remotely sensed time series of small reservoir surface areas, regional area-volume relations, publicly available rain records, and the model developed in this paper we can develop parameters to quantify reservoir storage. Despite different rain patterns in 2005 and 2006, our model, with the Thornthwaite-Mather parameters S_{max} and '*a*' that were determined in the year 2005, was able to predict runoff in 2006. Groundwater is seen to have no significant influence on reservoir storage during the filling period of the reservoirs, as it is too far below the surface (Edmonds, 1956), but may play a role in maintaining higher reservoir water levels once it has risen. The water filling small reservoirs is composed of rainfall directly on their surfaces, and quickflow from their watersheds. The results developed with our simple hydrological model are consistent with field-based studies. Therefore this approach is expected to be especially useful in data poor environments.

REFERENCES

Acheampong, P. K., 1988. Water Balance Analysis for Ghana. Geography 73, 125–131.

Edmonds, E. A., 1956. The Geology of the Bawku-Gambaga Area. Vol. Gold Coast Geological Survey Bulletin No. 19. Government of the Gold Coast, Accra.

Faulkner, J. W., Steenhuis, T., van de Giesen, N., Andreini, M., Liebe, J. R., 2008. Water use, and economic benefit of two small reservoir irrigation schemes in Ghana's Upper East Region. Irrigation and Drainage 57, 151–163.

Frazier, P. S., Page, K. J., 2000. Water Body Detection and Delineation with Landsat TM Data. Photogrammetric Engineering and Remote Sensing 66 (12), 1461–1467.

Gardini, B., Graf, G., Ratie, G., 1995. The Instruments on ENVISAT. Acta Astronautica 37, 301–311.

Jarvis, A., Reuter, H., Nelson, A., Guevara, E., 2006. Hole-filled seamless SRTM data V3. `http://srtm.csi.cgiar.org`.

Kranjac-Berisajevic, G., Bayorbor, T. B., Abdulai, A. S., Obeng, F., 1998. Rethinking Natural Resource Degradation In Semi-Arid Sub-Saharan Africa: The Case of Semi-Arid Ghana.

Liebe, J., van de Giesen, N., Andreini, M., 2005. Estimation of small reservoir storage capacities in a semi-arid environment. A case study in the Upper East Region of Ghana. Physics and Chemistry of the Earth 30, 448–454.

Liebe, J., van de Giesen, N., Andreini, M., Steenhuis, T. S., 2009. Suitability and limitations of ENVISAT ASAR for monitoring small reservoirs in a semi-arid area. IEEE Transactions on Geoscience and Remote Sensing.

Liu, B. M., Collick, A. S., Zeleke, G., Adgo, E., Easton, Z. M., Steenhuis, T. S., 2008. Rainfall-discharge relationships for a monsoonal climate in the Ethiopian highlands. Hydrological Processes 22 (7), 1059–1067.

Masiyandima, M. C., van de Giesen, N., Diatta, S., Windmeijer, P. N., Steenhuis, T. S., 2003. The hydrology of inland valleys in the sub-humid zone of West Africa: rainfall-runoff processes in the M'be experimental watershed. Hydrological Processes 17, 1213–1225.

McFeeters, S. K., 1996. The use of the Normalized Difference Water Index (NDWI) in the Delineation of open water features. International Journal of Remote Sensing 17 (7), 1425–1432.

Meigh, J., 1995. The impact of small farm reservoirs on urban water supplies in Botswana. Natural Resources Forum 19 (1), 71–83.

Mialhe, F., Gunnell, Y., Mering, C., 2008. Synoptic assessment of water resource variability in reservoirs by remote sensing: General approach and application to the runoff harvesting systems of south India. Water Resources Research 44.

Norman, W. R., Walter, M. F., 1993. Microsystems Irrigation in Niger, West Africa. Journal of Irrigation and Drainage Engineering 119 (5), 880–896.

Peranginangin, N., Sakthivadivel, R., Scott, N. R., Kendy, E., Steenhuis, T. S., 2004. Water accounting for conjunctive groundwater / surface water management: case of the Singkarak-Ombilin River basin, Indonesia. Journal of Hydrology 292 (1-4), 1–22.

Rawls, W. J., Brakensiek, D. L., Miller, N., 1983. Green-Ampt infiltration parameters from soils data. Journal of Hydraulic Engineering, Proceedings of the American Society of Civil Engineers 109 (1), 62–70.

Steenhuis, T. S., van der Molen, W. H., 1986. The Thornthwaite-Mather Procedure as a simple engineering method to predict recharge. Journal of Hydrology 84, 221–229.

Steenhuis, T. S., Winchell, M., Rossing, J., Zollweg, J. A., Walter, M. F., 1995. SCS runoff equation revisited for variable-source runoff areas. Journal of Irrigation and Drainage Engineering 121, 234–238.

Taylor, J. C., van de Giesen, N., Steenhuis, T. S., 2006. West Africa: Volta discharge data quality assessment and use. Journal of the American Water Resources Association 42 (4), 1113–1126.

Thornthwaite, C. W., Mather, J. R., 1955. The water balance. Publ. Climatol. 8 (1), 1–104.

van de Giesen, N., Stomph, T. H., de Ridder, N., 2000. Scale effects of Hortonian overland flow and rainfall-runoff dynamics in a West African catena landscape. Hydrological Processes 14, 165–175.

van de Giesen, N., Stomph, T. J., de Ridder, N., 2005. Surface runoff scale effects in West African watersheds: modeling and management options. Agricultural Water Management 72, 109–130.

White, M. E., 1978. Reservoir Surface Area from Landsat Imagery. Photogrammetric Engineering and Remote Sensing 44 (11), 1421–1426.

WMO, 2005. WHYCOS Guidlines. Hydrological information systems for integrated water resources management. WMO.

Xie, P., Arkin, P. A., 1997. A 17-year monthly analysis based on gauge observations, satellite estimates, and numerical model outputs. Bulletin of the American Meteorological Society 78 (11), 2539–58.

CHAPTER 3

LOCAL AND REGIONAL CONTROLS ON EVAPORATION FROM A SMALL RESERVOIR IN GHANA

3.1 Introduction

In the semi-arid regions of sub-saharan Africa, the climate is characterized by large inter-annual rainfall fluctuations, hard-to-predict rainy season onset, and variable rainfall patterns within the rainy seasons. This variability has a major impact on rain-fed agriculture and contributes to common drought-related crop failure during the rainy season. Small reservoirs provide a means to improve food security and local economies through irrigated agriculture in the dry season. The storage efficiency of small reservoirs, an important factor for their functioning, is affected by two primary sources of water loss: percolation (or seepage) and evaporation. While percolation losses are unwanted because water is lost from the reservoir, they do not constitute a water loss at a larger, watershed scale because the ”lost” water is transferred down-system where it supplies soil water or stream baseflow. Evaporation, in contrast, constitutes a real water loss from the landscape-watershed system. The common perception is that evaporation rates from these types of small reservoirs are immense because they are situated in a dry environment. Yet, there are few available, direct evaporation measurements from sub-tropical small reservoirs. Determining the evaporation losses is critically important to assessing the reliability of small reservoir water security, especially in arid landscapes where small reservoirs may constitute a substantial fraction of the regionally available water resources. The objectives of this chapter are to determine the evaporation from

a small reservoir in northern Ghana using direct and indirect measures, and to assess the evaporation-influencing interactions between the reservoir and the surrounding landscape and region.

3.2 Site Monitoring

The study site was a small reservoir located in the Upper East Region of Ghana (10°53' 20"N, 0°26'20"W, Figure 3.1). To obtain a direct measurement of reser-

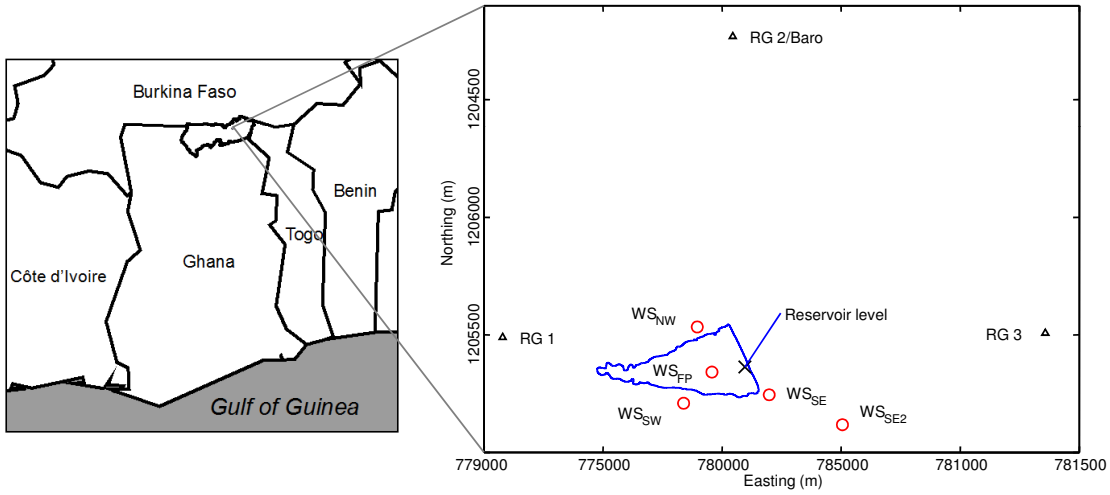

Figure 3.1: Study site and experimental setup.

voir evaporation, an automated floating evaporation pan (Figure 3.2) was developed and deployed on the reservoir. The float was triangular-shaped with a partially submerged class-A evaporation pan (121 cm in diameter, 25.4 cm deep) in its center. The pan's partial submergence was anticipated to reduce the enhanced heating problems common in terrestrial evaporation pans by dissipating energy into the reservoir water and, ideally, keeping the pan-water in thermal

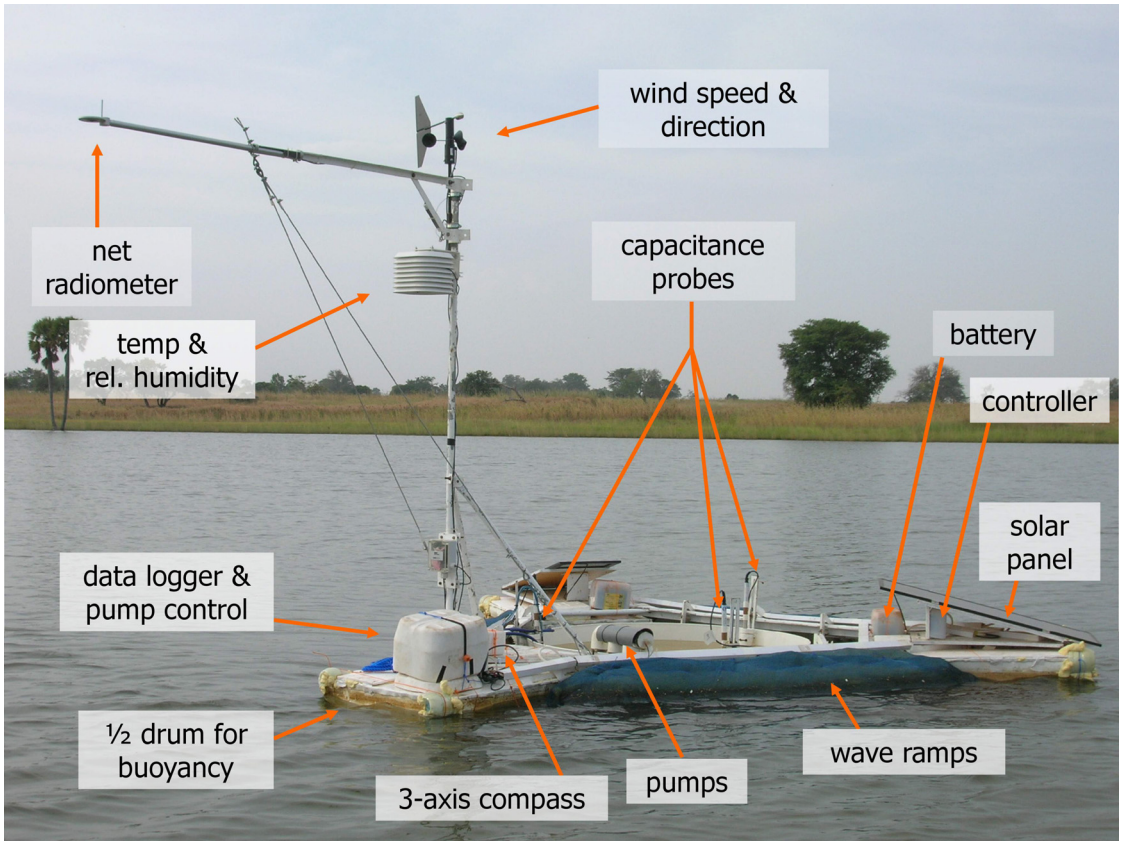

Figure 3.2: Automated floating evaporation pan.

equilibrium with the reservoir. The float frame and pan were made from white-painted metal. Buoyancy was attained with three sealed, half-barrels. A heavy, three bladed, star shaped, keel stabilized the structure. Along the float's sides, wave ramps were installed to dissipate wave energy and hinder splashing of water into the pan. The water level in the pan was measured in 64 sec intervals with three 250 mm long capacitance probes (Trutrak©, accuracy of $\pm$ 1 % of the full scale); note: one probe malfunctioned early in the study but differences among probe measurements were minute, which suggested good float stability. When evaporation drew the water level too low, the pan was automatically refilled by a 12-V bilge pump. Conversely, when rainfall filled the pan too deeply,

water was pumped out. The power for the data logger and the pumps was supplied through a 12-V photovoltaic system with two 14-W solar panels.

The float was also equipped with a weather station (WS_{FP}) to collect relevant meteorological data over the reservoir (Figure 3.2). Temperature and relative humidity were measured at 1.55 m above the water level and wind speed and wind direction were measured at 2 m. Net radiation was measured with a Kipp & Zonen NR-Lite net radiometer (a thermopile sensor with a 0.2-100 μ m spectral range; comparable to other net radiometers (Temesgen et al., 2007)) measured at 1.90 m over the water, and 1.65 m away from the edge of the float. The float was loosely anchored at three points to minimize spinning and keep the net radiometer boom oriented to the south. A three axis compass provided a reference for the wind direction sensor. All exposed metal parts of the raft frame were insulated with Styrofoam to reduce thermal "pollution." The reservoir's water temperature was measured at 10 cm, 100 cm and 175 cm depths every 15 minutes. The reservoir water level records were derived from a pressure transducer deployed at the deepest part of the reservoir and atmospheric pressure ('Baro') was measured close-by (Figure 3.1). Four additional, land based, weather stations were placed around the reservoir, measuring temperature, relative humidity, dew point, wind speed, and wind direction. Three stations were set-up $<$ 10 m from the full reservoir shoreline, along three axes separated by approximately 120°, to evaluate local up- and downwind effects. A fourth weather station was placed $\approx$ 330 m away from the full reservoir shoreline to compare evaporation rates from land and water. The weather stations were labeled according their position relative to the floating weather station WS_{FP} (WS_{NW}, WS_{SW}, WS_{SE}, and WS_{SE2}; Figure 3.1). Also, three tipping bucket rain gauges were deployed around the reservoir (Figure 3.1).

3.3 Evaporation Calculations

3.3.1 Pan evaporation

The evaporation from the floating pan was determined from measurements of water depth in the evaporation pan; 64 second interval data were aggregated to daily evaporation values by adding consecutive level differences. Data acquired during pump cycles and during rainfall events > 1 mm were omitted from the analysis. Land based pan evaporation (E_p) measurements usually exceeds lake evaporation due to the extra energy a pan receives through its sides and bottom (Jones, 1991). This is accounted for with a pan coefficient (Linacre and Geerts, 1997). Because our floating pan was partially submerged, we assumed the floating pan did not receive extra energy through its sides or bottom and, thus, no pan coefficient was applied to the floating evaporation pan measurements.

3.3.2 Reservoir Energy Balance

The energy balance is a common method to obtain reservoir evaporation (Vallet-Coulomb et al., 2001):

$$R_n = H + \lambda E + S \tag{3.1}$$

where R_n is the net radiation [W m^{-2}], H the sensible heat flux [W m^{-2}], λE the latent heat flux [W m^{-2}], λ is the latent heat of vaporization in [J kg^{-1}], E is the evaporation rate in [kg s^{-1} m^{-2}], and S is the change of energy stored in the lake [W m^{-2}].

A common simplifying approximation to the energy budget is made via the Bowen Ratio (Bowen, 1926):

$$\beta = \frac{H}{\lambda E} \, . \tag{3.2}$$

The advantage of using the Bowen Ratio is the assumption that it can be expressed in terms of temperature and vapor pressure (Brutsaert, 2005):

$$\beta = \gamma \frac{(T_s - T_a)}{(e_s - e_a)} \tag{3.3}$$

where γ is the psychrometric constant [hPa $^{\circ}C^{-1}$], *T* is temperature [°C], and *e* is the vapor pressure [hPa]; the subscripts *s* and *a* refer to surface and air measurements, respectively. The surface vapor pressure e_s is the saturated vapor pressure (e^*) at the surface temperature T_s, i.e. $e_s = e^*(T_s)$. Substituting the Bowen Ratio (Equation 3.2) into Equation 3.1 and converting evaporation from mass per area to depth yields

$$E_B = \frac{R_n - S}{\lambda(\beta + 1)} \left(\frac{1000}{\rho_w} \right) \tag{3.4}$$

where E_B is the Bowen-Ratio-based depth rate of evaporation [mm], and the temperature-dependent density of water, ρ_w, is calculated according to McCutcheon et al. (1993) with

$$\rho_w = 1000 \left(1 - \frac{T + 288.9414}{508929.2(T + 68.12963)(T - 3.9863)^2} \right) . \tag{3.5}$$

To calculate the heat content, Q_t [MJ m^{-2}], the reservoir was split into three layers, with the top layer covering the top 0.5 m, the second layer ranging from 0.5 to 1.5 m, and the third layer from 1.5 m to the bottom of the reservoir (thickness varying between 0.3 and 2.7 m depending on the reservoir fill level). Q_t was calculated with

$$Q_t = c_w \frac{1}{A_{0,t}} \sum_{n=1}^{3} T_{n,t} \, A_{n,t} \, h_{n,t} \tag{3.6}$$

where c_w is the volumetric specific heat of water (4.2 MJ m^{-3} K^{-1}), A_0 the surface area [m^2], T_n is the midpoint temperature [K] of a slice of thickness h_n [m], and a midpoint area A_n [m^2] (Wetzel and Likens, 1991).

After unit conversion, the energy flux into the reservoir (reservoir heat flux), S [W m^{-2}], is determined as the change over time in heat storage:

$$S = \frac{\Delta Q_t}{\Delta t} = \frac{Q_{t+\Delta t} - Q_t}{\Delta t} \tag{3.7}$$

where Δt is the measurement interval [s].

3.3.3 Penman evaporation from weather station data, and absolute humidity

The weather-station-based evaporation was calculated with the Penman (1948) equation:

$$E_t = \frac{\Delta}{\Delta + \gamma} Q_{ne} + \frac{\gamma}{\Delta + \gamma} E_A \tag{3.8}$$

where Δ is the slope of the saturation vapor pressure curve [hPa $°C^{-1}$], γ is the psychrometric constant [hPa $°C^{-1}$], and Q_{ne} is net available energy [mm h^{-1}] ((R_n-S)/λ). E_A is commonly referred to as the drying power of the air, and is defined by:

$$E_A = f_e(e_{a^*} - e_a) \tag{3.9}$$

where the saturation vapor pressure deficit (a.k.a. saturation deficit) is calculated as the difference between the air's saturation vapor pressure, e_{a^*} [hPa], and the air's actual vapor pressure, e_a [hPa]. The term f_e in Equation 3.9 is the so-called wind function; despite many suggested forms (e.g., Penman (1948), 1956, Cohen et al. (2002)), we assumed $f_e = 0.268(0.54u)$, as proposed by Linacre

(1993) specifically for open water evaporation (referenced in Valiantzas (2006)), where *u* is the wind speed [m s^{-1}], and 0.268 is a unit conversion factor (Allen et al., 2005). As the constants require that E_A is in mm d^{-1}, hourly values were obtained by dividing E_A by 24.

Absolute humidity, *aH* [g m^{-3}] was calculated from *rH* [%], temperature *T* [°C], dewpoint temperature T_d [°C], and barometric pressure [hPa] records:

$$aH = \frac{(e_a m_w)}{((273+T)R/1000)} \tag{3.10}$$

where m_w is the molecular weight of water (m_w=18.02 g mol^{-1}), *R* is the gas constant (*R* = 8.314472 Pa m^{-3} $mol^{-1}K^{-1}$), and the actual vapor pressure e_a [hPa] was calculated with

$$e_a = 6.11 \times 10^{(7.5\ T_d)/(237.7+T_d)}\ . \tag{3.11}$$

3.3.4 Energy advection

In cases where wet areas are surrounded by extensive dry areas, these wet areas can experience excessive evaporation losses due to energy advection. This situation is sometimes also referred to as the oasis effect (Oke, 1987). The ”extra” energy is supplied from the surrounding atmosphere, which is also indicated through the negative sensible heat flux, *H*, and negative Bowen Ratio, β, during this time. The conditions for the energy advection are met, when

$$\textit{advection} = \frac{\lambda E}{R_n} > 1 \bigwedge H < 0\ . \tag{3.12}$$

3.4 Results

3.4.1 Floating pan evaporation, E_o

The daily evaporation rates determined from the floating evaporation pan, E_o, fluctuated widely (Figure 3.3). The long gap between March and August 2006

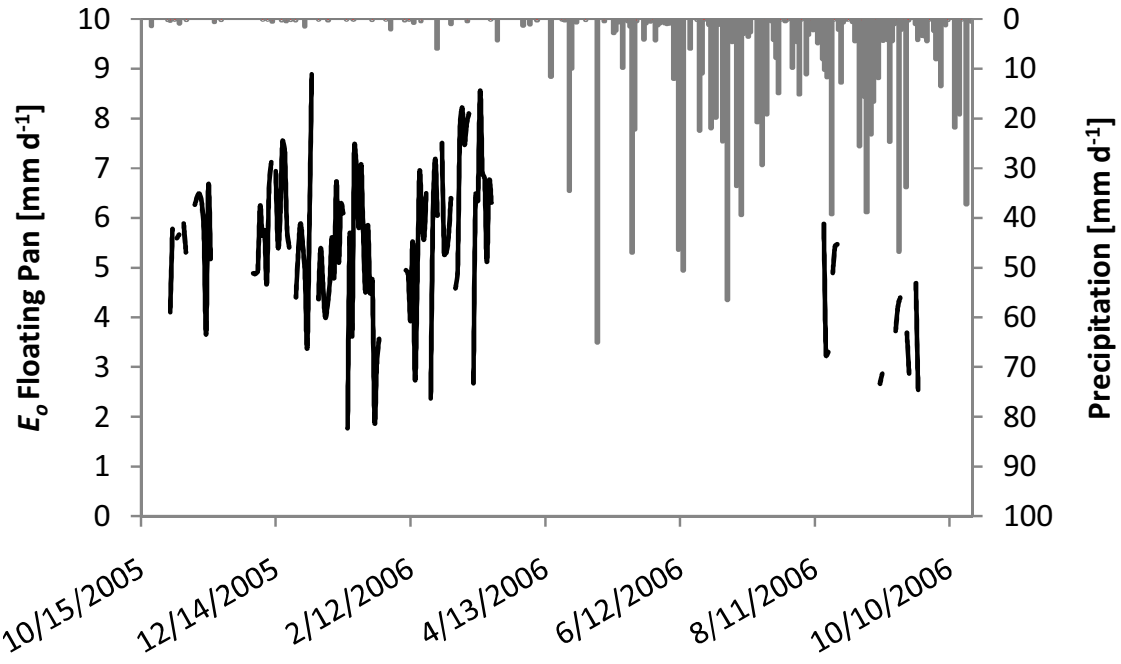

Figure 3.3: Daily floating pan evaporation (heavy black lines), and average daily precipitation (grey vertical lines) during the study period.

is due to a sensor malfunction, the other gaps are due to data omission on days with pump cycles. The average monthly E_o values are given in Table 3.1. The evaporation rates are high during the dry season with mean daily rates ranging from 5.8 mm in November to 6.5 mm in March, which is typically the driest month in this region. During the rainy season, the measured evaporation rates

are significantly lower, ranging between 4.4 mm d^{-1} in September 2006, and 4.8 mm d^{-1} in August 2006 respectively.

3.4.2 Reservoir Energy balance, E_B, and Penman E_t

For each month, the mean daily energy-budget-based evaporation, E_B (Equation 3.4), the magnitudes of the components of the reservoir's energy budget, and the potential evaporation, E_t, after Penman (Equation 3.8) are given in Table 3.1.

The energy budget shows that, from October 2005 until (at least) March 2006, the energy used for evaporation, λE, exceeds the net radiative energy input, R_n. In these months, energy is advected to the reservoir, and the condition stated in Equation 3.12 is met. The "extra" energy is supplied from the surrounding atmosphere, which is also indicated through the negative sensible heat, H, and negative Bowen Ratio, β, during this time.

The monthly mean E_B values range from 6.3 mm d^{-1} in January 2006 to 7.8 mm d^{-1} in February and March 2006. Similarly, the evaporation rates determined on the floating pan (WF_{FP}) with Penman, E_t, are slightly above the pan measurements, E_o. E_t ranged from 6 mm d^{-1} in January and August 2006 to 7.5 mm d^{-1} in March 2006. The land based Penman evaporation rates, $E_{t\ Land}$ determined at (WF_{SE2}) range from 5.8 mm d^{-1} in January 2006 to 7.6 mm d^{-1} in September 2006.

Table 3.1: Components of the reservoir's energy budget, E_o, E_B, Penman E_t over water, and Penman $E_{t\ Land}$.

Month	R_n	$R_n - S$	λE	H	β	$\lambda E/(R_n - S)$	E_o	E_B	E_t	$E_{t\ Land}$
	[W m^{-2}]	[W m^{-2}]	[W m^{-2}]	[W m^{-2}]	[-]	[-]	[mm d^{-1}]	[mm d^{-1}]	[mm d^{-1}]	[mm d^{-1}]
Oct 2005	142.4	134.3	152.8	-18.5	-0.2	1.1	5.2	6.9	6.4	6.0
Nov 2005	157.4	148.1	189.8	-41.7	-0.2	1.3	5.8	6.5	6.1	6.2
Dec 2005	147.0	135.4	199.1	-63.7	-0.3	1.5	5.7	6.6	6.4	6.1
Jan 2006	150.5	150.5	213.0	-63.7	-0.3	1.4	5.0	6.3	6.0	5.8
Feb 2006	187.5	182.9	238.4	-55.6	-0.2	1.3	5.6	7.8	7.3	7.4
Mar 2006	194.4	193.3	241.9	-48.6	-0.2	1.3	6.5	7.8	7.5	7.5
...	...	...	...	...	...	...	...	...	...	...
Aug 2006	210.6	210.6	192.1	17.4	0.1	0.9	4.8	6.7	6.0	6.9
Sep 2006	228.0	228.0	209.5	18.5	0.1	0.9	4.4	7.5	6.6	7.6

Energy advection from October to March ($\lambda E/R_n > 1 \bigwedge H < 0$)

3.5 Discussion

3.5.1 Comparison of E_o, E_B, and E_t

Evaporation rates determined both with the energy budget, E_B, and with Penman, E_t, exceeded the evaporation rates determined with the floating evaporation pan, E_o (Figure 3.4).

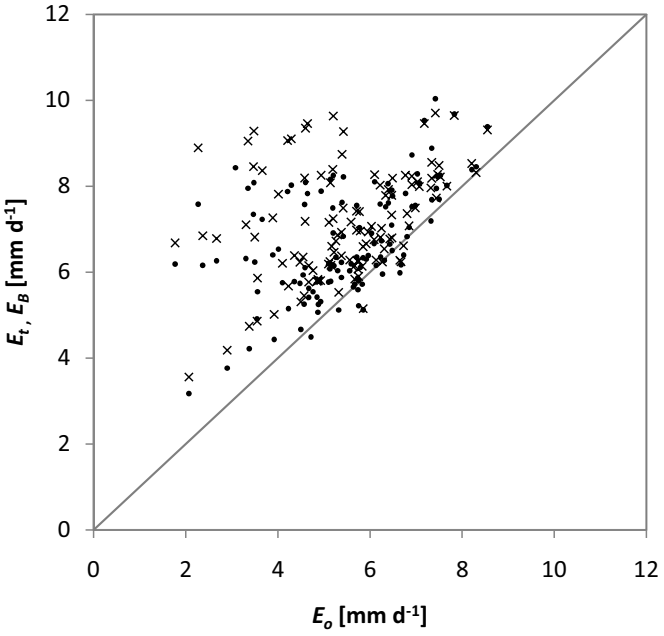

Figure 3.4: Comparison of daily E_o with E_B (x's), and E_t (dots)

The comparison of E_B and E_t shows that these two measurements are in good agreement (r^2 = 0.92, *MAE* [1] = 0.5 mm, σ=1.3 mm^2). Comparing daily E_B and E_t rates (Figure 3.5) shows that evaporation rates determined with E_B are slightly higher than the E_t rates. The spread of the two evaporation measurements increases slightly with the overall magnitude of evaporation.

[1]Mean Absolute Error, $MAE = \frac{1}{n}\sum_{i=1}^{n}|f_i - y_i|$, where f_i is the predicted value and y_i is the true value for each data pair *i* of a total of *n* measurements

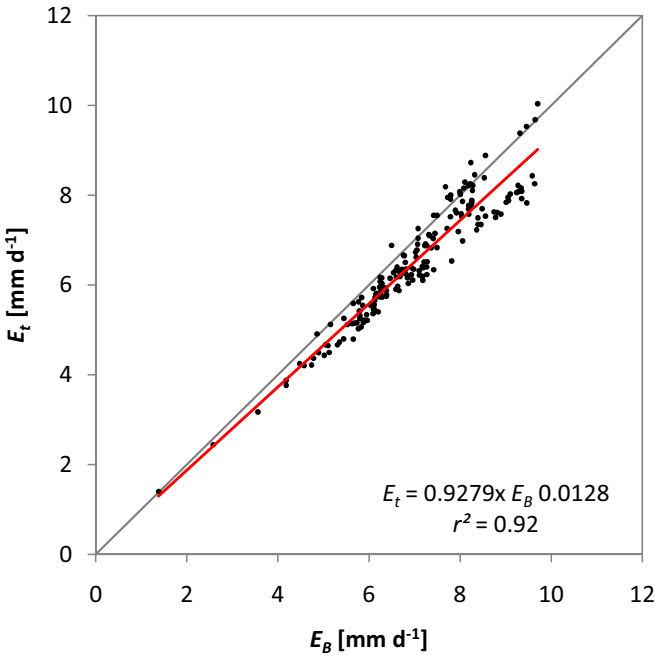

Figure 3.5: Comparison of daily E_B and E_t for the reservoir at WS_{FP}

Comparing E_t measured over water with $E_{t\ Land}$ determined at WS_{SE2} indicates that evaporation losses from small reservoirs are not excessive. The daily values presented in Figure 3.6 show very little discrepancy between the E_t rates over water, and $E_{t\ Land}$.

3.5.2 Comparison of reservoir surface water temperature, and pan water temperature

An immediate question in the explanation of the differences in evaporation rates between the pan E_o and E_B or E_t concerns temperature differences betwee the pan water and the reservoir surface water, i.e. whether the pan is in thermal equilibrium with the reservoir. Between 11/30/2005 and 2/2/2006 both sur-

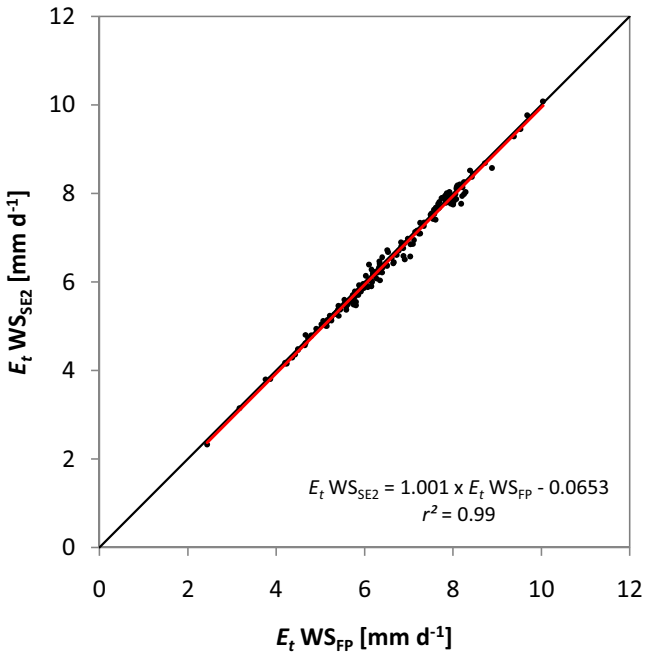

Figure 3.6: Comparison of daily E_t over water (at WS$_{FP}$) with E_t over land (at WS$_{SE2}$)

face water temperature and pan water temperature were measured. Figure 3.7 shows that the pan water temperature has a higher amplitude than the reservoir surface water measurement, but the difference between their 24h moving averages (smooth red line for pan water temperature, and smooth blue line for surface water temperature) are very small. It can be concluded that the pan does not show much thermal pollution, although the greater amplitude of the pan water temperature suggests that it captured the reservoir surface temperature better compared to the dampened signal from surface water temperature measurement that was recorded slightly deeper.

The E_B and E_t rates presented in the previous section were calculated using water surface temperature measured at 10 cm depth in the reservoir, which affects the paramters ρ_w, λ, β, e^*, and S. Due to the similarity in the 24h moving

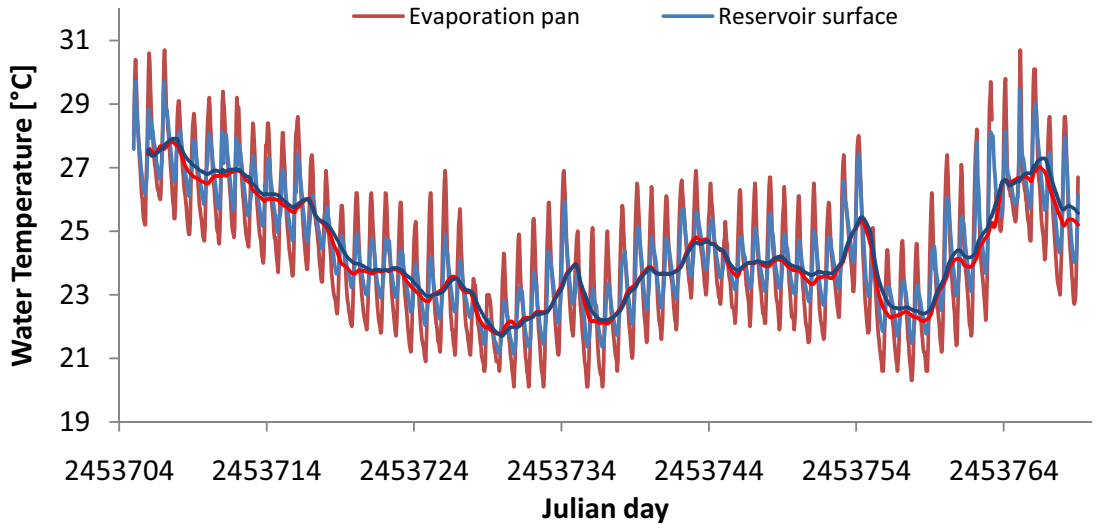

Figure 3.7: Pan water (hourly in dark red, 24h moving average in red) and reservoir surface water (hourly in light blue, 24h moving average in dark blue) temperatures.

averages (Figure 3.7) the effect of this is minimal. Figure 3.8 shows the difference in E_B calculated with pan water temperature, and surface water temperature from 11/30/2005 and 2/2/2006. E_B calculated with the surface water temperature is, on average, 0.2 mm d^{-1} above E_B calculated with pan water temperature.

3.5.3 Upwind and downwind effects at weather stations

Figure 3.9 shows the distribution of wind speeds and directions for the study period; the highest speed and most frequent winds are from the SW, followed by the NE. Winds from NW or SE are very rare. The following section discusses the evaporation dynamics observed at the reservoirs under these predominant wind directions, i.e. the SW monsoon, and the NE trade winds.

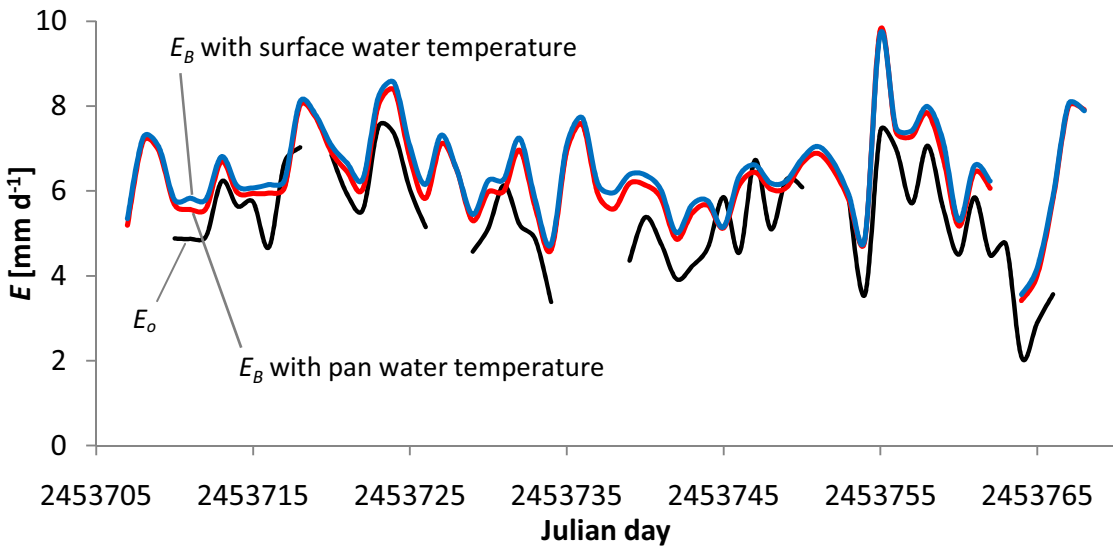

Figure 3.8: The effect of surface water and pan water temperature on E_B.

With the setup of weather stations around the reservoir we are able to address up-and downwind effects at the different weather stations around the reservoir. The comparison of absolute humidity values of weather station pairs provides information the vapor concentration or density in the air [g H_2O m^{-3}], which is independent of possible temperature differences that may exist between the land and water based weather stations. Another, related, important factor for evaporation losses is the saturation deficit [%] (i.e. 100-rH), which is an indication of the drying power of the air.

The density scatterplots in Figures 3.10 a, 3.11 a, and 3.12 a, compare absolute humidity measurements from the floating weather station, WS_{FP}, and a land based weather station, WS_{NW} or WS_{SW}. The values of the upwind weather station are plotted on the x-axis, and the values of the downwind weather station on the y-axis. In Figures 3.10 and 3.12, the land based weather station is upwind of the floating weather station, whereas in Figure 3.11 the land based

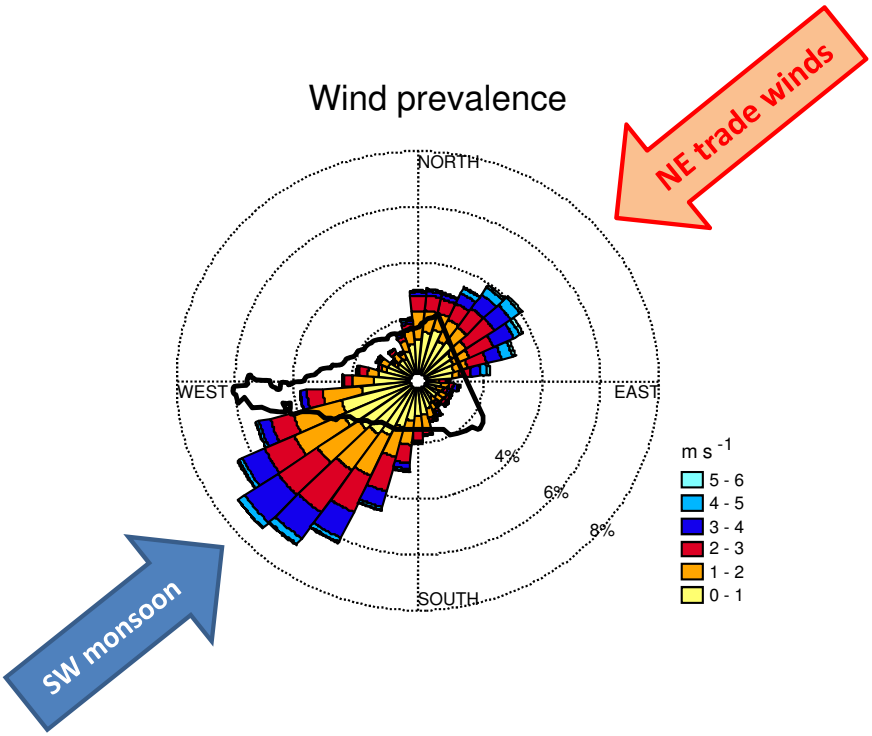

Figure 3.9: Local wind direction and speed prevalence patterns. The length of wind rose wedges correspond to the prevalence of wind from that direction. The colored subsections indicate wind speed frequencies.

weather station is downwind from the reservoir. Figures 3.10 b, 3.11 b, and 3.12 b, give an indication of the saturation deficits, their frequency, and the wind directions considered in the above graphs (Figures 3.10 a, 3.11 a, and 3.12 a), in form of wind roses. The total length of the wedges show the relative frequency of the wind directions, and their color coded subdivisions represent the frequency of the saturation deficit at the depicted weather stations at the given wind directions. The reservoir outlines overlain on the wind roses, and the indication of the position of the floating weather station WS_{FP} (circle), facilitate the understanding of the up- and downwind situations.

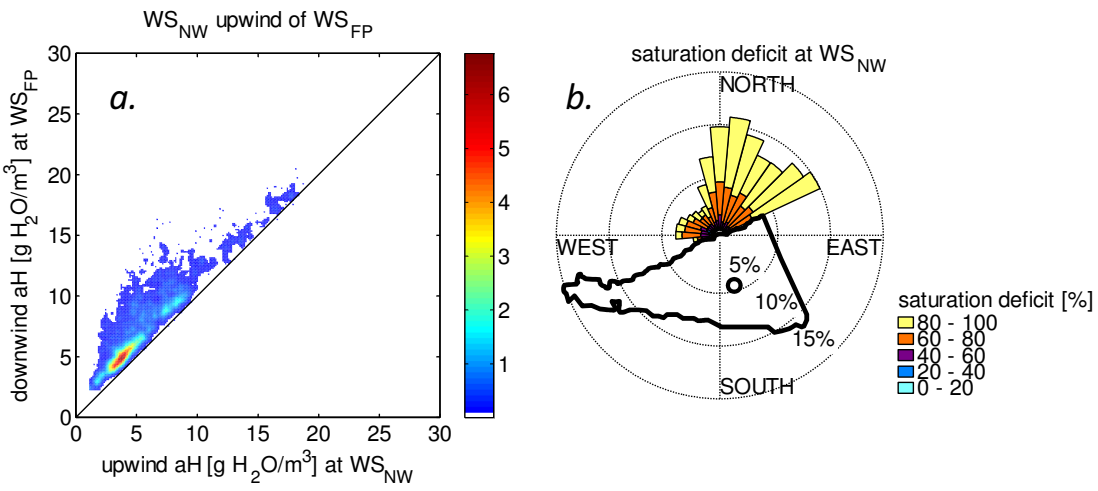

Figure 3.10: *aH* scatterplot (a) and saturation deficit (b) when WS_{NW} is in upwind position of WS_{FP} (cirlce in (b)).

Figure 3.10 a shows that with NE winds, the air is generally very dry. Most of the air coming from NE directions (x-axis) carries less than 10 g H_2O m^{-3}; a minor concentration forms at 3 g H_2O m^{-3}. The respective absolute humidity measurements on the reservoir (WS_{FP}, y-axis) are all higher, and cluster above the parity line, which is a clear indication that evaporation takes place. In cases when more saturated air, with absolute humidity levels greater than 10 g H_2O m^{-3}, approaches weather station WS_{NW} (y-axis), the moisture pick-up becomes less pronounces, and the data in the scatterplot converges closer to the parity line. The reason for the evaporation losses also becomes apparent in Figure 3.10 b, which indicates that NE winds are most frequently associated with very pronounced saturation deficits.

Figure 3.11 a depicts data comparing absolute humidity measurements from the weather station southwest of the reservoir, WS_{SW}, with those recorded at WS_{FP} under NE winds, i.e. when the land based weather station is downwind

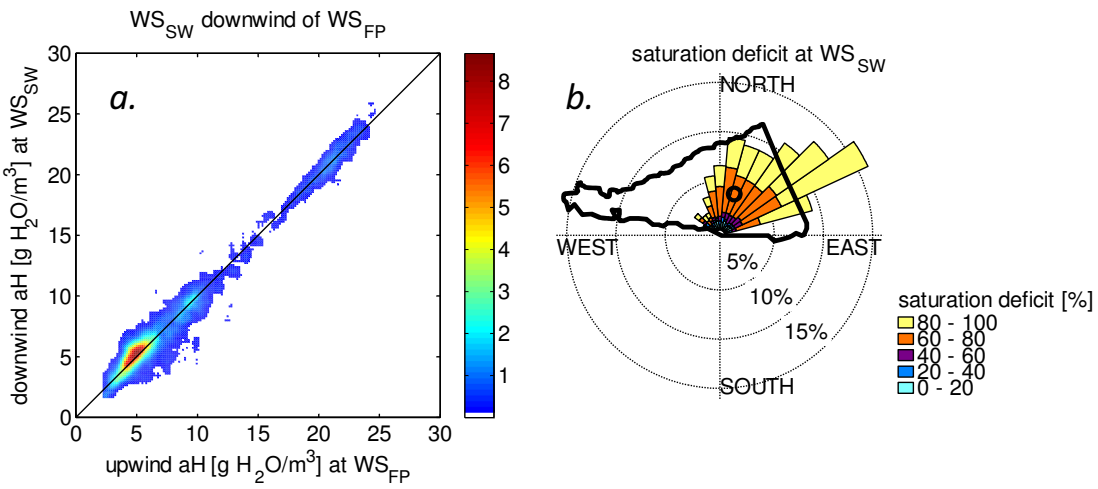

Figure 3.11: *aH* scatterplot (a) and saturation deficit (b) when WS_{SW} is in downwind position of WS_{FP} (cirlce in (b)).

from the reservoir. The greatest concentration forms at 5 g H_2O m^{-3}, above the parity line, which indicates that there is still some more uptake of moisture between WS_{FP} and WS_{SW}, but not as pronounced as between WS_{NW} and WS_{FP} under similar wind conditions (3.10 a). In situations where the air already contains substantial quantities of water, the difference in absolute humidity between the two weather stations is minute. Overall, the values lie much closer to the parity line compared to Figure 3.10 a. The wind rose for WS_{SW} (3.11 b) shows that, similarly to Figure 3.10 b, NE winds most often have a high saturation deficit, although less distinct than at the upwind weather station (3.10 b).

Figure 3.12 a depicts the comparison of weather station WS_{SW} in upwind position of WS_{FP}, i.e. under SW winds. Most frequently, the absolute humidity of the air approaching the reservoir is very high, with a concentration at 22 g H_2O m^{-3}. While in Figures 3.10 a and 3.11 a the highest concentration is slightly

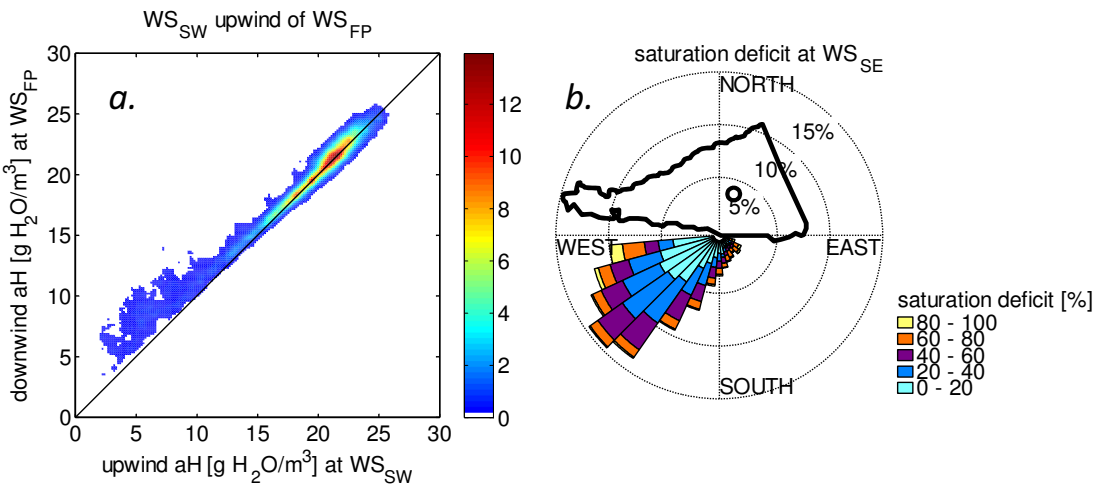

Figure 3.12: *aH* scatterplot (a) and saturation deficit (b) when WS_{SW} is in upwind position of WS_{FP} (cirlce in (b)).

above the parity line, the highest concentration in Figure 3.12 a is *on* the parity line, indicating that in most cases there is little additional evaporation under these conditions. Significant evaporation only occurs when the initial moisture content of the air is low. Below 10 g H_2O m^{-3} at WS_{SW}, the entire point cloud moves above the parity line. Figure 3.12 b affirms that under SW winds, the saturation deficit of the arriving air masses is generally very low, such that the air can pick up only little additional moisture from the open water body.

3.6 Conclusion

The storage efficiency of this study's small reservoir was perhaps better than common dogma would suggest. Indeed, evaporation rates from the reservoir, measured with the floating evaporation pan, E_o, were generally lower than the evaporation determined with the Bowen Ratio method, E_B, or Penman E_t. To

explain this difference, ”thermal pollution” of the pan water was ruled out. It may be speculated that, despite its low profile, the floating pan was shielded by the pan walls and the raft structure, but proof of this speculation would require further, detailed analysis of the effect of the floating pan on the flow of air masses over the pan. E_B and E_t over water, computed with Linacre's (1993) wind function, were in good agreement. Similarly, the comparison of water and land based E_t and $E_{t\ Land}$ showed almost no difference. Excessive evaporation losses, compared to the surrounding landscape, were not apparent.

The analysis of absolute humidity changes between the land and water based weather stations under different wind directions shows that evaporation losses from a reservoir are not uniform (Figures 3.10a and 3.11a). On the upwind edge of a reservoir, evaporation losses are much more pronounced than on the downwind edge. This is most apparent when the the saturation deficit of the approaching air is high.

Our study demonstrated that regional wind patterns play important roles in the annual evaporation dynamics from the reservoir. The peak evaporation rates occur during the dry season from November until May, when NE winds dominated. These winds are associated with high saturation deficits (Figures 3.10 b and 3.11 b). The most frequent wind direction, however, is SW (Figure 3.9), which is generally associated with low saturation deficits (Figure 3.12 b), and therefore little capacity to pick up additional water vapor from the reservoir. Peak evaporation losses are therefore clearly seasonally concentrated, to the period when NE winds prevail.

REFERENCES

Allen, R. G., Walter, I. A., Elliot, R. L., Howell, T. A., Itenfisu, D., Jensen, M. E., 2005. The ASCE Standardized Reference Evapotranspiration Equation. American Society of Civil Engineers, Reston, VA.

Bowen, I. S., 1926. The ratio of heat losses by conduction and by evaporation from any water surface. Physics Review 27, 779–787.

Brutsaert, W., 2005. Hydrology. Cambridge University Press, Cambridge.

Cohen, S., Ianetz, A., Stanhill, G., 2002. Evaporative climate changes at Bet Dagan, Israel, 1964-1998. Agricultural and Forest Meteorology 111 (2), 83–91.

Jones, F. E., 1991. Evaporation of Water: with Emphasis on Applications and Measurements. Lewis Publishers, Inc, Chelsea, Michigan.

Linacre, E., Geerts, B., 1997. Climates and Weather explained. Routledge, London.

Linacre, E. T., 1993. Data-sparse estimation of lake evaporation, using a simplified Penman equation. Agricultural and Forest Meteorology 64 (3-4), 237–256.

McCutcheon, S., Martin, J., Barnwell, T. J., 1993. Water Quality. In: Maidment, D. (Ed.), Handbook of Hydrology. McGraw-Hill, New York, p. 11.3.

Oke, T. R., 1987. Boundary Layer Climates, 2nd Edition. Routledge, London.

Penman, H. L., 1948. Natural evaporation from open water, bare soil and grass. Proceedings of the Royal Society of London Series a-Mathematical and Physical Sciences 193 (1032), 120–145.

Penman, H. L., 1956. Evaporation: An introductory survey. Neth. J. Agric. Sci. 4, 9–29.

Temesgen, B., Eching, S., Frame, K., 2007. Comparing net radiation estimation methods: CIMIS versus Penman-Monteith. Journal of Irrigation and Drainage Engineering-Asce 133 (3), 265–271.

Valiantzas, J. D., 2006. Simplified versions for the Penman evaporation equation using routine weather data. Journal of Hydrology 331 (3-4), 690–702.

Vallet-Coulomb, C., Legesse, D., Gasse, F., Travi, Y., Chernet, T., 2001. Lake evaporation estimates in tropical Africa (Lake Ziway, Ethiopia). Journal of Hydrology 245 (1-4), 1–18.

Wetzel, R. G., Likens, G. E., 1991. Limnological Analyses, 2nd Edition. Springer-Verlag, New York.